PAPER

CeNTREX: a new search for time-reversal symmetry violation in the ²⁰⁵Tl nucleus

To cite this article: O Grasdijk et al 2021 Quantum Sci. Technol. 6 044007

View the article online for updates and enhancements.

You may also like

 Teleseismic P-wave tomography and the upper mantle structure of the Sulu orogenic belt (China): implications for Triassic collision and exhumation mechanism

Miao Peng, Handong Tan, Mei Jiang et al.

- Design of optimal stimulation patterns for neuronal ensembles based on Volterratype hierarchical modeling
 V Z Marmarelis, D C Shin, R E Hampson et al.
- Rational material design of mixed-valent high-T_c superconductors
 Z. P. Yin and G. Kotliar



IOP ebooks™

Bringing together innovative digital publishing with leading authors from the global scientific community.

Start exploring the collection-download the first chapter of every title for free.

Quantum Science and Technology



RECEIVED

1 October 2020

REVISED

8 November 2020

ACCEPTED FOR PUBLICATION 15 January 2021

PUBLISHED
2 September 2021

PAPER

CeNTREX: a new search for time-reversal symmetry violation in the ²⁰⁵Tl nucleus

O Grasdijk^{1,*}, O Timgren¹, J Kastelic¹, T Wright^{1,6}, S Lamoreaux¹, D DeMille^{1,2,3,*}, K Wenz⁴, M Aitken⁴, T Zelevinsky⁴, T Winick⁵ and D Kawall⁵

- ¹ Department of Physics, Yale University, New Haven, CT 06511, United States of America
- Physics Division, Argonne National Laboratory, Argonne, IL 60439, United States of America
- James Franck Institute and Department of Physics, University of Chicago, Chicago, IL 60637, United States of America
- Department of Physics, Columbia University, New York, NY 10027-5255, United States of America
- Department of Physics, University of Massachusetts Amherst, Amherst, MA 01003, United States of America
- * Authors to whom any correspondence should be addressed.
- ⁶ Present address: JILA, National Institute of Standards and Technology and University of Colorado, and Department of Physics, Boulder, Colorado 80309, United States of America

E-mail: olivier.grasdijk@yale.edu and ddemille@uchicago.edu

Keywords: CP violation, Schiff moment, cold molecules, atomic physics, new-physics

Abstract

The Cold molecule Nuclear Time-Reversal EXperiment (CeNTREX) is a new effort aiming for a significant increase in sensitivity over the best present upper bounds on the strength of hadronic time reversal (T) violating fundamental interactions. The experimental signature will be shifts in nuclear magnetic resonance frequencies of 205 Tl in electrically-polarized thallium fluoride (TlF) molecules. Here we describe the motivation for studying these T-violating interactions and for using TlF to do so. To achieve higher sensitivity than earlier searches for T-violation in TlF, CeNTREX uses a cryogenic molecular beam source, optical state preparation and detection, and modern methods of coherent quantum state manipulation. Details of the measurement scheme and the current state of the apparatus are presented, with quantitative measurements of the TlF beam. Finally, the estimated sensitivity and methods to control systematic errors are discussed.

1. Introduction

Before the early 1960s, it was believed that *CP* is a good symmetry of nature. As Landau pointed out, that would make it impossible for particles to have electric dipole moments (EDMs) along their spin axis [1]. The detection of such an EDM would thus provide clear evidence of *CP*-violation (CPV).

While most processes preserve *CP*, certain weak interactions violate it as observed in *K*-, *B*-, and *D*-meson decays [2, 3]. The flavor-changing part of the standard model (SM) quark sector includes a CPV phase in the CKM quark-mixing matrix [4]. This so-called Kobayashi–Maskawa mechanism introduces the third quark generation to explain the CPV [5]. The CKM phase has been the only source of observed CPV so far [3].

A major motivation for CPV searches comes from the baryon asymmetry of the Universe (BAU). Compared to the current baryon density $n_{\rm B}$, the antibaryon density $n_{\rm B}$ is very small; the reported upper bounds for the antimatter-to-matter number ratio range from 10^{-15} to 10^{-6} [6]. To date, no mechanism has been experimentally verified that can explain the BAU. In a 1967 paper, Sakharov argued that CPV is necessary to explain the BAU [7] if the initial conditions of the Universe were *C*-symmetric. The existing CPV in the CKM matrix is not enough to explain the extent of the BAU [8]. Thus new sources of CPV are required to explain the BAU.

No flavor-neutral CPV signal has been observed yet. However, many mechanisms can lead to such phenomena. For example, the QCD Lagrangian can, in principle, include an effective CPV term, proportional to the parameter $\bar{\theta}$ [9]:

$$\mathcal{L} = \bar{\theta} \frac{g^2}{32\pi^2} G^a_{\mu\nu} \widetilde{G}^a_{\mu\nu},\tag{1}$$

where G^a is the gluon field tensor, g is the strong coupling constant, and $\bar{\theta}$ is dimensionless. Experimental limits from experiments searching for CPV in neutral ¹⁹⁹Hg atoms [10] and ultracold neutrons [11, 12] suggests that the strength of this term relative to the usual strong interaction is $|\bar{\theta}| < 9 \times 10^{-11}$. The unexplained smallness of $\bar{\theta}$ is known as the strong CP problem. One proposed solution to the strong CP problem is the so called Peccei–Quinn mechanism, with an accompanying elementary scalar particle: the axion [13]. The axion would naturally lead to $\bar{\theta} \approx 0$, and is an attractive candidate for dark matter [14–16]. (A review of experimental searches for the axion is given in [17]).

New hadronic *CP*-violating interactions from the QCD sector, or from physics beyond the SM, can lead to an effective charge asymmetry along the spin of a particle. Such charge asymmetries include EDMs and, for finite size particles such as nuclei, Schiff moments [18]. In the SM, EDMs and nuclear Schiff moments (NSMs) are induced by the CKM phase, but are strongly suppressed: an EDM cannot appear below the three-loop level for quarks, or four-loop for leptons [19]. The CKM phase can produce a proton or neutron EDM no larger than 10^{-32} e cm. Proposed extensions to the SM carry new CPV phases, which may manifest as EDMs or NSMs larger than expected based on the SM. The search for an EDM or NSM thus constitutes a nearly background-free signal for new physics. In fact, the background expected from the SM would only become apparent when probing effects beyond the energy scale of $\sim 10^5$ TeV [8].

At present, searches for EDMs and related phenomena give the most sensitive constraints on flavor-neutral CPV effects beyond the SM. However, these searches are subject to the following limitation. According to the Schiff theorem, the interaction energy of nonrelativistic point-charged electric dipoles, bound in a neutral system but subject to an arbitrary external electrostatic potential, has no term linear in the CPV charge distribution [18]. Physically, the system rearranges itself so as to screen the external field completely [20]. Thus, a *CP*-violating moment of a charged constituent in a bound system cannot be detected without some mechanism to bypass Schiff's theorem. Two such mechanisms are relativistic constituent motion and finite constituent size.

A nucleus in an atom or molecule is nonrelativistic, but has an extended size. This finite size can lead to a residual electromagnetic moment, the Schiff moment S, that gives rise to a CP-violating interaction. In heavy diamagnetic atoms and diatomic molecules such as TIF, this finite-size effect gives the dominant contribution to CPV signals. Since the nuclear spin I is the only preferred direction in a nucleus, S has to lie parallel to this axis, i.e. S = SI/I. This quantum Schiff moment has the symmetries of I: it changes sign under time reversal (T) but not under parity (P). By contrast, the classical Schiff moment is a static charge distribution that is unchanged under T but changes sign under P. Hence, a nonzero value of S means that both T and P symmetries are violated. On the assumption that CPT is a good symmetry, a nonzero value of S thus is also a signature of CPV.

The Schiff moment corresponds to a charge displacement that is similar to an EDM in its asymmetric distribution along the spin axis. It is equivalent to a charge density on the nuclear surface proportional to $\cos \theta$, where θ is the angle from **I**; this surface charge distribution produces a uniform electric field inside the nucleus [21]. The magnitude *S* of the NSM scales with the atomic mass *A* as $S \propto A^{2/3}$ [22].

The value of S can be related to more fundamental CP-violating parameters, including CPV π meson–nucleon interaction constants \bar{g}_0 , \bar{g}_1 , and \bar{g}_2 ; the $\bar{\theta}$ QCD parameter; quark chromo-EDMs \tilde{d}_d and \tilde{d}_u ; and the neutron and proton EDMs, d_n and d_p . For example, the NSM of the ²⁰⁵Tl nucleus⁷ can be written as [23, 24]:

$$S(^{205}\text{Tl}) \approx (0.13g\bar{g}_0 - 0.004g\bar{g}_1 - 0.27g\bar{g}_2) \text{ e fm}^3;$$

$$S(^{205}\text{Tl}) \approx 0.027\bar{\theta} \text{ e fm}^3;$$

$$S(^{205}\text{Tl}) \approx (12\tilde{d}_d + 9\tilde{d}_u) \text{ e fm}^2;$$

$$S(^{205}\text{Tl}) \approx 0.4d_p \text{ fm}^2.$$
(2)

If detected, a nonzero $S(^{205}\text{Tl})$ would provide evidence for a nonzero value of one or more of these fundamental CPV parameters.

Energy shifts associated with an NSM can be greatly enhanced in polar molecules, where there is another intrinsic direction in addition to the nuclear spin: the internuclear axis $\hat{\bf n}$. In TIF, we define $\hat{\bf n}$ as pointing from F to Tl, associated with the internal molecular dipole moment and a corresponding strong intramolecular gradient of the electron density. For nuclei inside a molecule, the NSM (and other

⁷ The 205 Tl nucleus has closed neutron shells; hence its NSM has negligible contribution from $d_{\rm n}$.

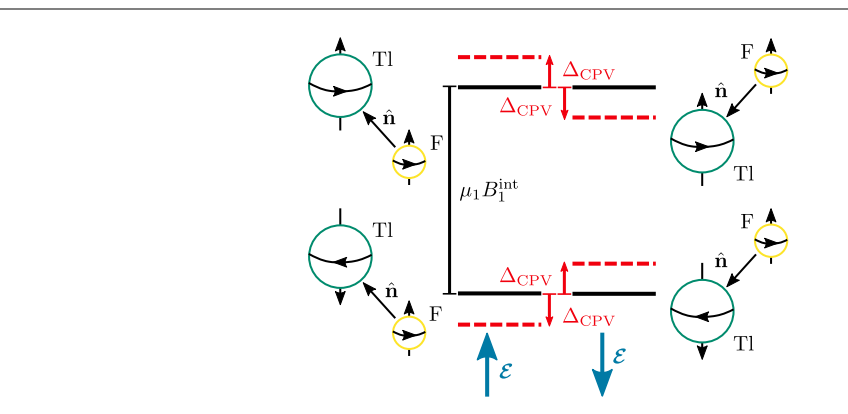


Figure 1. T-violating energy shift $\Delta_{\text{CPV}} = W_S S \mathcal{P}$ as a result of a nonzero NSM S given by the effective interaction $\mathcal{H}_{\text{CPV}} = W_S S \mathbf{I} \cdot \hat{\mathbf{n}} / I$ (equation (3)), shown for opposite orientations of the applied field \mathcal{E} . Here μ_1 is the Tl magnetic moment and B_1^{int} is the effective internal magnetic field at the Tl nucleus due to the spin–rotation interaction.

CP-violating effects [22]) interacts with this density gradient, giving rise to an effective CPV Hamiltonian of the form [23]

$$\mathcal{H}_{\text{CPV}} = W_{S} S \frac{\mathbf{I}}{I} \cdot \hat{\mathbf{n}}. \tag{3}$$

Here, W_S is the proportionality constant between S and the CPV contribution to the molecular energy, for a fully polarized molecule. Its value is determined by the properties of the electronic wavefunctions, which can be calculated from first principles [23, 25–27]. The magnitude of W_S grows rapidly with atomic number Z of the nucleus, as $W_S \propto Z^2$ [28].

Without an external electric field \mathcal{E} , the interaction of equation (3) fails to produce a first-order effect in any given energy eigenstate. This is because the rotation of the molecule averages $\hat{\mathbf{n}}$ to zero, and the expectation value $\langle \mathcal{H}_{CPV} \rangle$ vanishes [29, 30]. However, when an external field is applied, the molecule becomes polarized and both $\hat{\mathbf{n}}$ and \mathcal{H}_{CPV} acquire non-zero expectation values, with $\langle \hat{\mathbf{n}} \rangle \| \mathcal{E}$. We define the degree of electrical polarization $\mathcal{P} \equiv \langle \hat{\mathbf{n}} \cdot \hat{\mathcal{E}} \rangle$, (where $\hat{\mathcal{E}} = \mathcal{E}/\mathcal{E}$), so that $-1 \leqslant \mathcal{P} \leqslant 1$. Hence, energy shifts due to CPV are given by $\langle \mathcal{H}_{CPV} \rangle = W_S \mathcal{P} \hat{\mathcal{E}} \cdot \frac{1}{1}$.

Polar molecules can be polarized readily in laboratory-scale fields owing to their small rotational level separation ($\sim 10^{-4}$ eV), giving them near-maximal energy shifts induced by a given Schiff moment. Thus, Sandars [31] suggested a molecular-beam resonance experiment could be used to probe the existence of the proton EDM, if the molecule has a heavy atom with an unpaired proton in the nucleus, such as 205 Tl. The value of S is determined by measuring energy splittings between spin-up and -down states relative to $\langle \hat{\mathbf{n}} \rangle$ (which is parallel to the applied electric field \mathcal{E}). This splitting will increase or decrease as \mathcal{E} (and hence $\langle \hat{\mathbf{n}} \rangle$) reverses, due to the interaction in equation (3). The difference in level splittings is proportional to the electric polarization \mathcal{P} , the interaction strength W_S , and S (figure 1).

CeNTREX uses a cold beam of thallium fluoride (TIF) to measure nuclear T-violation due to the NSM of the 205 Tl nucleus. It is a suitable system to look for P- and T-violating interactions for a number of reasons: a molecular beam of TIF can be readily obtained; many of the molecular states and transitions are known experimentally; the species is a polar diatomic molecule, enhancing the electron density gradient at the site of the nuclei (and hence W_S). As the thallium nucleus is heavy (A = 205, Z = 81) and the NSM-induced energy shift scales $\propto A^{2/3}Z^2$, the observable effect of the Tl Schiff moment is correspondingly large [31, 32]. Since the Tl nucleus contains an unpaired proton, CeNTREX will be primarily sensitive to proton EDM effects, as opposed to other leading experiments which are more sensitive to the neutron EDM [10]. TIF is not very sensitive to the electron EDM due to its zero total electron spin [33].

The current best constraint on T-violating interactions associated with $S(^{205}\text{Tl})$ was found by Cho, Sangster and Hinds in 1991 [29, 30], who measured an NSM-induced frequency shift of $\Delta E = 2\Delta_{\text{CPV}} = (1.4 \pm 2.4) \times 10^{-4}$ Hz, consistent with zero⁸. Using the effective interaction \mathcal{H}_{CPV} , the shift in the energy splitting between states with Tl spin up versus spin down, relative to the quantization axis, can be interpreted as

$$\Delta E = 2\Delta_{\text{CPV}} = 2W_{\text{S}}S\operatorname{sgn}(\mathcal{E})\mathcal{P},\tag{4}$$

⁸ Throughout, we express both frequencies and energies in linear frequency units (Hz), and all angular momentum operators are treated as dimensionless.

where $W_S = 40\,539$ a.u., polarization $\mathcal{P} = \langle \hat{\mathbf{n}} \cdot \hat{\boldsymbol{\mathcal{E}}} \rangle = 0.547$, and the sign of \mathcal{E} refers to the direction of \mathcal{E} relative to a fixed quantizing axis \hat{z} . This determines the Schiff moment [24, 26]

$$S(^{205}\text{Tl}) = (3.6 \pm 6.1) \times 10^{-11} \text{ e fm}^3.$$
 (5)

With equation (2), the following limits can be placed:

$$\bar{\theta} = (1.3 \pm 2.3) \times 10^{-9},$$

$$12\bar{d}_{\rm d} + 9\bar{d}_{\rm u} = (3.6 \pm 6.1) \times 10^{-24} \text{ cm}$$

$$d_{\rm p} = (0.9 \pm 1.5) \times 10^{-23} \text{ e cm},$$

$$0.13g\bar{g}_0 - 0.004g\bar{g}_1 - 0.27g\bar{g}_2 = (3.6 \pm 6.1) \times 10^{-11}.$$
(6)

Centrex aims to improve on these limits by using a cryogenic molecular beam source to achieve a cold beam with higher intensity and lower velocity spread compared to the jet source used in the previous work. Rotational cooling will be performed with optical and microwave pumping, collapsing much of the initial Boltzmann distribution into one state, greatly enhancing the number of molecules accessible for measurement. Finally, optical cycling will be used to assist state readout, resulting in near-unity detection efficiency. Fluorescence detection, compared to the hot-wire techniques used previously, allows for background-free detection if scattered light is well controlled.

1.1. Thallium fluoride

The TIF molecule is described by its electronic, vibrational and rotational motion, plus the states of the TI and F nuclear spins. CeNTREX makes use of states both in the vibronic ground state, $X^1\Sigma^+$ ($\nu=0$), and in an electronically excited state, $B^3\Pi_1$ ($\nu=0$). In both cases, we describe the angular momentum couplings in a Hund's case (a) basis. We typically write energy eigenstates in terms of the basis states $|\eta, J, F_1, F, m_F\rangle$. Here, η represents the vibronic quantum numbers; J is the total angular momentum excluding the nuclear spins, $F_1 = J + I_1$, with $I_1 = 1/2$ for 205 TI; $F = F_1 + I_2$ is the total angular momentum, with $I_2 = 1/2$ for 19 F; and m_F is its projection along a quantization axis in the lab frame. Field-free eigenstates are close to these basis states in the ground $X^1\Sigma^+$ state. In the $B^3\Pi_1$ state, strong hyperfine interactions significantly mix states with different J and F_1 values. Hence, we describe these eigenstates with the modified notation $|\eta', \widetilde{J}', \widetilde{F}_1', F', m_F'\rangle$, where \widetilde{J}' and \widetilde{F}_1' correspond to the largest component in their basis-state decomposition; the primes indicate that the ket refers to the excited state $B^3\Pi_1$.

Molecules in the beam are assumed to be in the vibronic ground state, since the beam temperature is much lower than the energy scales associated with the electronic and vibrational excitations. However, even at cryogenic temperatures, there is a Boltzmann distribution over many rotational and nuclear spin states. The dominant term in the energy of rotational/spin levels in the $X^1\Sigma^+$ state is due to rotation; the mean energy of states with quantum number J is $E_{\rm rot} = BJ(J+1)$, where $B \approx 6.67$ GHz ≈ 0.3 K $k_{\rm B}$, where $k_{\rm B}$ the Boltzmann constant.

Hyperfine interactions split sublevels with different F values (F = J - 1, J, J, J + 1, except F = 0, 1 only for J = 0) in each rotational state. Thus, each rotational level has 4(2J + 1) magnetic sublevels. Including rotation, spin–rotation and spin–spin interactions, plus interactions with external electric (\mathcal{E}) and magnetic (\mathcal{B}) fields, the system is described by the effective Hamiltonian [32] $\mathcal{H}_{TIF} = \mathcal{H}_{rot} + \mathcal{H}_{sr} + \mathcal{H}_{ss} + \mathcal{H}_{S} + \mathcal{H}_{Z}$, where

$$\mathcal{H}_{\text{rot}} = B\mathbf{J}^{2}$$

$$\mathcal{H}_{\text{sr}} = c_{1}(\mathbf{I}_{1} \cdot \mathbf{J}) + c_{2}(\mathbf{I}_{2} \cdot \mathbf{J}),$$

$$\mathcal{H}_{\text{ss}} = c_{3}T^{2}(\mathbf{C}) \cdot T^{2}(\mathbf{I}_{1}, \mathbf{I}_{2}) + c_{4}(\mathbf{I}_{1} \cdot \mathbf{I}_{2}),$$

$$\mathcal{H}_{S} = -\mu_{e} \cdot \mathcal{E},$$

$$\mathcal{H}_{Z} = -\frac{\mu_{J}}{J}(\mathbf{J} \cdot \mathcal{B}) - \frac{\mu_{1}}{I_{1}}(\mathbf{I}_{1} \cdot \mathcal{B}) - \frac{\mu_{2}}{I_{2}}(\mathbf{I}_{2} \cdot \mathcal{B}).$$

$$(7)$$

Here, the first term in the spin–spin interaction (\mathcal{H}_{ss}) contains the scalar product of two rank-2 tensors: one constructed from the modified spherical harmonics C, and one from I_1 and I_2 [36]. (The matrix

⁹ In Ramsey *et al* [32], the symbol *B* denotes the rotational constant in equilibrium position, i.e. there $B \equiv B_e$. However, the effective $\nu = 0$ rotational constant, B_0 , is more relevant to CeNTREX. To first order in the Dunham expansion [34], $B_0 = B_e - \alpha_e/2$. With B_e and A_e from the NIST database [35], we find B_0 . We define the symbol $B \equiv B_0$; its value is shown in table 1.

Table 1. Constants describing rotational, hyperfine, Zeeman, and Stark interactions in the effective TIF ground-state Hamiltonian (equation (7)). All values taken from Ramsey *et al* [32], except for *B* (see section 1.1).

B = 6.66733 GHz	$\mu_e = 4.2282(8)$ Debye
$\mu_I = 35(15) \mathrm{Hz}\mathrm{G}^{-1}$	$c_1 = 126.03(12) \text{ kHz}$
$\mu_1^{205} = 1.2405(3) \mathrm{kHz}\mathrm{G}^{-1}$	$c_2 = 17.89(15) \mathrm{kHz}$
$\mu_1^{203} = 1.2285(3) \text{ kHz G}^{-1}$	$c_3 = 0.70(3) \text{ kHz}$
$\mu_2 = 2.00363(4)~\rm kHz~G^{-1}$	$c_4 = -13.30(72) \text{ kHz}$

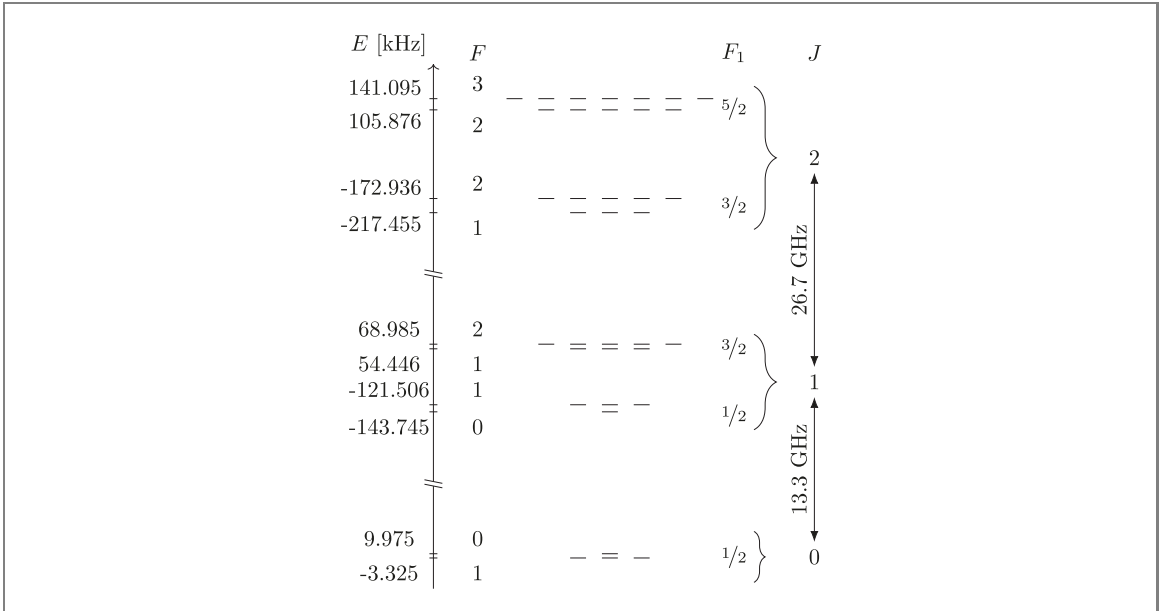


Figure 2. Hyperfine structure in the lowest three rotational levels in the TIF ground state $X^1\Sigma^+$, with no applied fields. Rotational energies hBJ(J+1) should be added to the hyperfine energy shifts indicated on the axis. Note the (2F+1)-fold degeneracy of each state with total angular momentum F, corresponding to the quantum numbers $m_F = -F, \ldots, 0, \ldots, F$.

elements diagonal in J of this term are given in [32].) The hyperfine parameters c_1, c_2, c_3, c_4 , rotational constant B, magnetic moments μ_J , μ_1 , μ_2 , and molecule-frame EDM μ_e are all known from previous measurements; their values are given in table 1. A level diagram of low-lying states in the absence of applied fields is shown in figure 2.

In CeNTREX, lasers are tuned to $X^1\Sigma^+(\nu=0)\to B^3\Pi_1~(\nu=0)$ transitions in order to manipulate and read out ground state hyperfine and rotational sublevels. Details of the $B^3\Pi_1$ state structure are given in [37, 38]. Here, only a few main features of the B state substructure are important. First, the B state hyperfine splittings are very large (\gtrsim 100 MHz) compared to the natural linewidth of the transition ($\gamma_B\approx 1.6$ MHz), which is in turn much larger than the ground-state hyperfine splittings ($c_j\lesssim 100$ kHz). This means that hyperfine structure is fully resolved in the excited state, and entirely unresolved in the ground state. Hence, optical transitions in TlF drive a large manifold of ground-state hyperfine levels (with a given value of J) to a single hyperfine state with (nominal) quantum numbers \tilde{J}, \tilde{F}_1 and exact quantum number F. Another important feature of the B state is that its matrix of Franck–Condon factors (FCFs) for decay to the X state is extremely diagonal [39], such that $\sim 99\%$ of the time, the $B(\nu=0)$ vibronic state decays back to the vibronic ground state $X(\nu=0)$. This enables optical pumping and optical cycling with little loss. However, the mixing of J and F_1 by the strong B-state hyperfine interaction substantially modifies rotational selection rules in B-X decays, and must be taken into account when describing optical excitation and emission in TlF.

1.2. TIF in \mathcal{E} -fields

Throughout most of the CeNTREX apparatus, TIF molecules experience a non-zero \mathcal{E} -field and (nominally) zero \mathcal{B} -field. The character of the energy eigenstates changes significantly depending on the \mathcal{E} -field magnitude, which varies dramatically between stages of the experiment. Hence, it is useful to describe the energy eigenstates of the TIF electronic ground state in different regimes of \mathcal{E} -field strength (with $\mathcal{B}=0$), as defined by the ratio of Stark shifts, $\Delta E_{\rm S}=\langle\mathcal{H}_{\rm S}\rangle\sim\mu_e^2\mathcal{E}^2/B$, to the strength of hyperfine interactions, $E_{\rm hf}=\langle\mathcal{H}_{\rm sr}+\mathcal{H}_{\rm ss}\rangle\sim c_j$, or rotational energies, $E_{\rm rot}=\langle\mathcal{H}_{\rm rot}\rangle\sim B$. In all regimes, the total angular momentum projection m_F along a space-fixed quantization axis \hat{z} (always defined such that $\boldsymbol{\mathcal{E}}$ is very nearly parallel to \hat{z}), is an exact quantum number.

Table 2. Regimes of electric field strength and associated eigenstates in TIF.

Regime	Definition	Field strength	Approx. eigenstates				
Low Mid High	$\begin{split} \Delta E_{\rm S} &\ll E_{\rm hf} \\ E_{\rm hf} &\ll \Delta E_{\rm S} \ll E_{\rm rot} \\ E_{\rm hf} &\ll E_{\rm rot} \lesssim \Delta E_{\rm S} \end{split}$	$\begin{split} \mathcal{E} &\lesssim 50 \text{ V cm}^{-1} \\ 50 \text{ V cm}^{-1} &\ll \mathcal{E} \lesssim 5 \text{ kV cm}^{-1} \\ 5 \text{ kV cm}^{-1} &\ll \mathcal{E} \end{split}$	$ \begin{array}{l} J,F_{1},F,m_{F}\rangle \\ J,m_{J}\neq0\rangle \left m_{I_{1}},m_{I_{2}}\rangle \right J,m_{J}=0\rangle \left I_{t},m_{I_{t}}\rangle \\ \left \widetilde{J},m_{J}\neq0\right\rangle \left m_{I_{1}},m_{I_{2}}\rangle \right \widetilde{J},m_{J}=0\rangle \left I_{t},m_{I_{t}}\rangle \end{array} $				

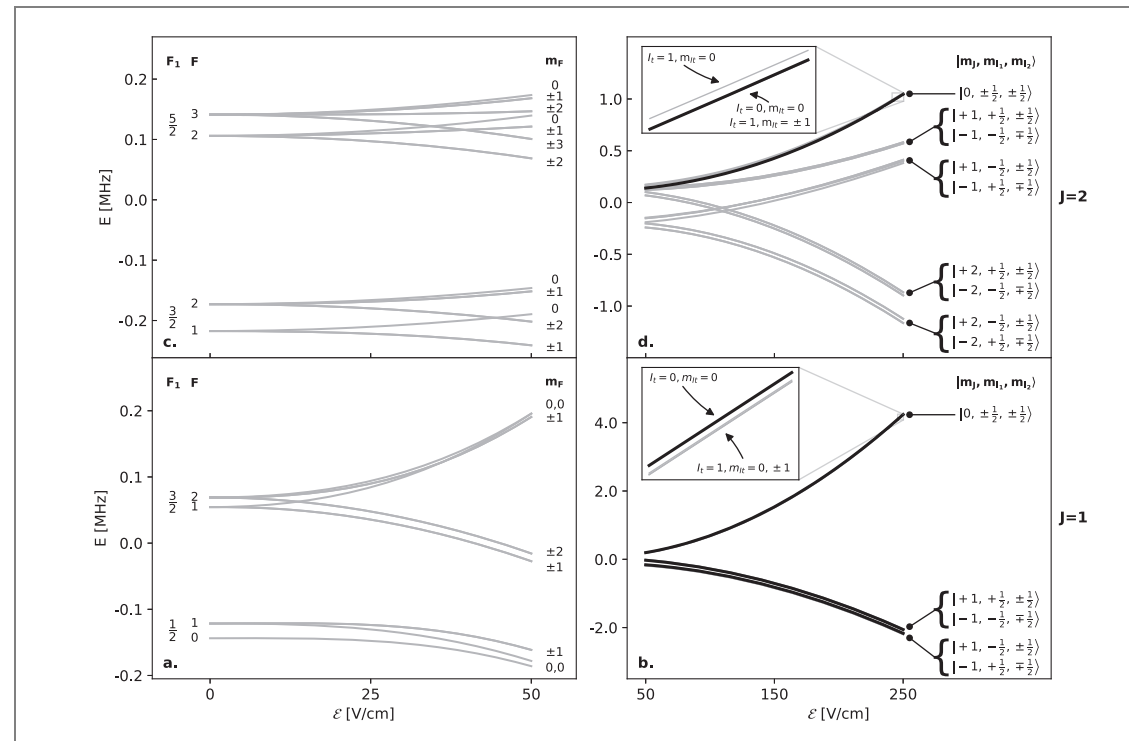


Figure 3. Overview of the energy eigenstates for changing \mathcal{E} -field magnitudes. The low-field regime, where $\Delta E_S \ll E_{hf}$, where energy eigenstates retain J, F, and F_1 as approximate quantum numbers is shown in (**a**) for J=1 and (**c**) for J=2. The mid-field regime, where $E_{hf} \ll \Delta E_S \ll E_{rot}$, where both J and m_J are approximate quantum numbers is shown in (**b**) for J=1 and (**d**) for J=2. States used in CeNTREX are shown in bold.

In the low-field regime, where $\Delta E_{\rm S} \ll E_{\rm hf}$, energy eigenstates retain J, F, and F_1 as approximate quantum numbers. In the mid-field regime, where $E_{\rm hf} \ll \Delta E_{\rm S} \ll E_{\rm rot}$, both J and m_J are approximate quantum numbers. Here, the tensor part of the Stark shifts gives rise to energy splittings between levels with different values of $|m_J|$ that are comparable in size to the scalar shifts, i.e. of order $\Delta E_{\rm S}$. Thus, when $m_J \neq 0$, J is strongly coupled to \mathcal{E} (and hence to the molecular axis $\hat{\mathbf{n}}$) by this Stark interaction. In this case, each nuclear spin is coupled to J (and thus also to \mathcal{E}) by the spin–rotation interactions of $\mathcal{H}_{\rm sr}$. Hence, here m_{I_1} and m_{I_2} are approximate quantum numbers. By contrast, in states where $m_J = 0$ (including when J = 0) in this regime, $\langle \mathcal{H}_{\rm sr} \rangle$ vanishes to first order, and the nuclear spins do not couple to J and \mathcal{E} . However, the nuclear spins remain coupled to each other via the spin–spin interaction $\mathcal{H}_{\rm ss}$. So, here the total nuclear spin $I_{\rm t} = I_1 + I_2$ and its projection $m_{I_{\rm t}}$ are approximate quantum numbers in addition to J and $m_J = 0$. Finally, in the high-field regime where $E_{\rm hf} \ll E_{\rm rot} \lesssim \Delta E_{\rm S}$, J states are strongly mixed, and separations between m_J states are on the order of $E_{\rm rot}$. Here, eigenstates are defined by the same approximate quantum numbers as in the mid-field regime, aside from J. We refer to these strongly mixed states with the label \widetilde{J} , which corresponds to the value of J that any given state connects to adiabatically, if the \mathcal{E} -field is reduced. Table 2 summarizes the different regimes and associated eigenstates.

Figure 3 shows how the relevant energies and eigenstates evolve from the low-field to the mid-field regime for J = 1 and J = 2 states. Bold curves are states directly relevant to CeNTREX. Figure 4 shows a zoom out of states up to J = 2 from low to high fields.

The 205 Tl NSM measurement is carried out in $\tilde{J}=1, m_J=\pm 1$ states of TlF at large electric field $\mathcal{E}=30~\mathrm{kV~cm^{-1}}$. This choice of states takes advantage of the structure of TlF in electric fields, in two ways. First, the observable energy shift associated with S, ΔE , scales linearly with the degree of polarization \mathcal{P} of the TlF molecule (equation (4)). An electric field more easily polarizes states with low J, since \mathcal{P} arises from mixing between states with different parity and thus different J; these states are closest together when J is small. Additionally, as discussed in section 3.4, certain dangerous systematic errors in the NSM

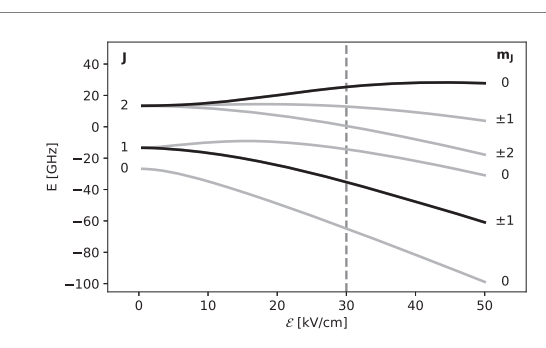


Figure 4. Evolution of the energy eigenstates of the TIF Hamiltonian (equation (7)) for \mathcal{E} ranging from 0 V cm⁻¹ to 50 kV cm⁻¹, for J = 0, 1, 2. States used in CeNTREX are shown in bold. Hyperfine structure is unresolved in this plot.

measurement are dramatically suppressed in the presence of a strong spin–rotation interaction (later referred to as an effective intra-molecular magnetic field). This requires $m_J \neq 0$. The $\tilde{J} = 1$, $m_J = \pm 1$ states hence provide the best combination of sensitivity and systematic error suppression in TIF¹⁰.

2. Experiment overview

CeNTREX consists of a series of modules. In this section we describe each region and its function, following the path of a typical TIF molecule in the experiment. A cryogenic buffer gas beam source (BS) forms a cold, slow, and bright molecular beam. Next, a rotational cooling region (RC) accumulates molecules from the many thermally populated states into a single hyperfine state in J = 0. Next, the molecules are coherently transferred from J = 0 to J = 2, $m_I = 0$ in state preparation region A (SPA). This makes it possible to focus the molecular beam at a final detection region downstream with the electrostatic quadrupole lens (EQL). State preparation region B (SPB) coherently moves population from $J=2, m_I=0$ to $J=1, m_I=\pm 1$, the states used for the Schiff moment measurement. Next, the main interaction region (MI) performs nuclear magnetic resonance (NMR) in the presence of a strong polarizing \mathcal{E} -field using the technique of separated oscillatory fields (SOF) [40, 41]. A short RF magnetic field subregion creates a superposition of thallium nuclear spin states. After a period of free precession in \mathcal{E} , a second RF field subregion maps the phase accumulation due to the energy difference of the spin states—including a contribution from the Schiff moment—into a population difference between the spin states. In state preparation region C (SPC), each spin state is transferred to a different rotational state. Finally, the rotational populations are read out with laser-induced fluorescence (LIF) and optical cycling in the fluorescence detection region (FD). An overview of the beamline design is shown in figures 5 and 6.

Because the quantizing fields in CeNTREX change direction throughout the apparatus, we find it useful to use two different coordinate systems. We use (X, Y, Z) to denote 'beamline' coordinates, where \hat{Z} points in the average direction of the molecular beam and \hat{Y} is vertical upward. Similarly, we use (x, y, z) to denote 'interaction region' coordinates. Here, \hat{z} lies along a line parallel to the average \mathcal{E} -field in the interaction region, $\langle \mathcal{E} \rangle_{\text{MI}}$, \hat{x} is the vector closest to the average beam velocity that is also perpendicular to \hat{z} , and \hat{y} is the vector closest to downward (along gravity) that is perpendicular to \hat{z} and \hat{x} . The direction of \hat{z} (parallel or antiparallel to $\langle \mathcal{E} \rangle_{\text{MI}}$) is fixed in the lab, set by the definitions of \hat{x} and \hat{y} and by demanding a right-handed coordinate system. Hence, the \mathcal{E} field in the MI region is (nominally) $\mathcal{E} = \mathcal{E}\hat{z}$, where \mathcal{E} can take either sign.

2.1. Beam source

The source of the TIF molecules is a cryogenic neon buffer gas beam [42]. A copper cell containing a solid TIF target is cooled to 18 K. The TIF is ablated with a pulsed Nd:YAG laser operating at up to 50 Hz, while Ne flows continuously through the cell at a typical rate of 40 sccm. A 4 K layer surrounds the cell and cryopumps the Ne. Ablated TIF reaches thermal equilibrium with the Ne buffer gas before the cell exit, where the beam cools further as it expands into vacuum. The cold cell aperture (6.35 mm diameter) defines the zero position along the beamline axis, **Z**. Two 25.4 mm diameter apertures (one in the 4 K layer at Z = 43 mm, one in a blackbody shield at Z = 81 mm) collimate the beam.

The velocity distributions of the TIF beam were measured as follows. An additional collimator was placed downstream. After this collimator, a laser beam, tuned to a Q1 line of the X-B transition, crossed

 $^{^{10}}$ $|\mathcal{P}|$ is larger in the J=0, $m_J=0$ states, given the same \mathcal{E} -field value. Hence, the NSM gives larger energy shifts there. However, in these states where $m_J=0$, the effective intra-molecular magnetic field vanishes.

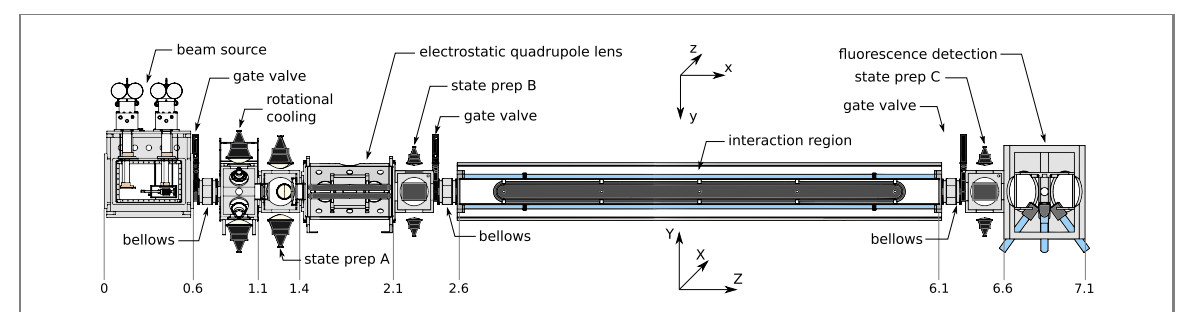


Figure 5. Overview of the planned CeNTREX beamline. Distance in meters is shown on the bottom. Modules following the EQL are currently being designed, so few details are given.

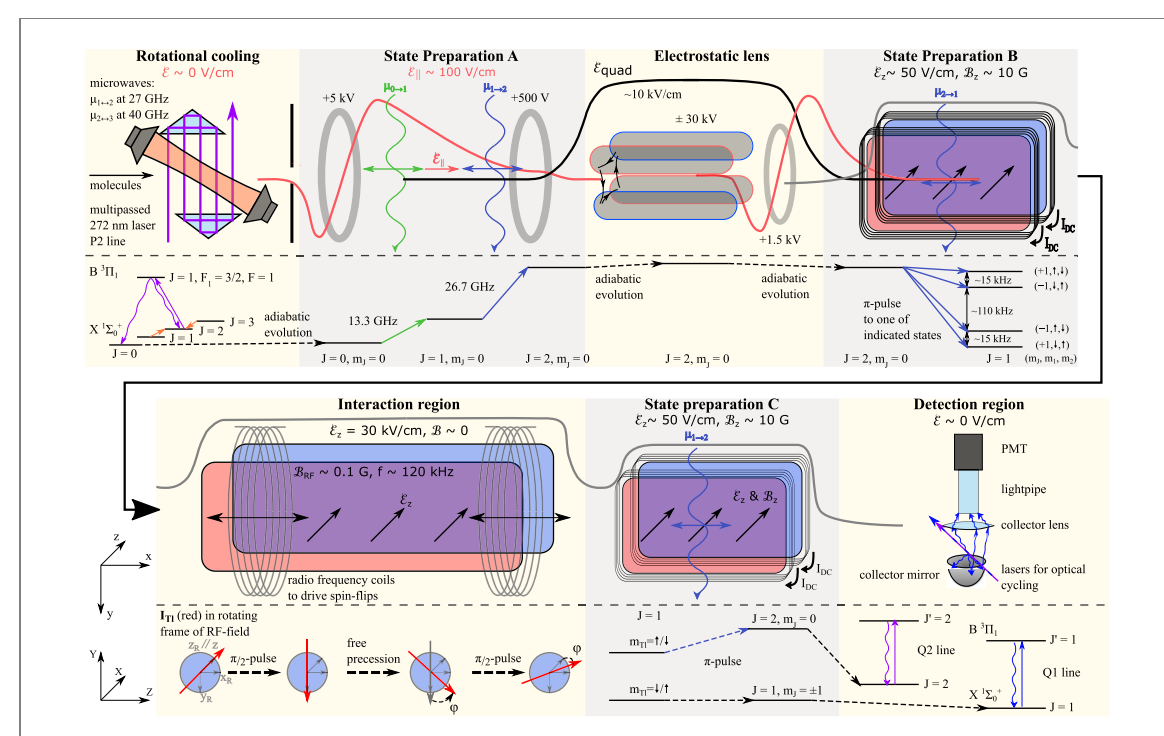


Figure 6. Overview of the regions the TIF molecules traverse as they move through the CeNTREX beamline. After emerging from the beam source (not shown), the molecules enter the rotational cooling region. Here, the population in the rotational levels J=1,2, and 3 is optically pumped to $|J=0,F=0\rangle$. (See section 2.2 and figure 8 for more detail.) From there, they move into SPA, where adiabatic passage (AP) is applied twice to transfer the molecules to $|J=2,m_J=0\rangle$ (section 2.3), the state focused by the electrostatic lens (section 2.4). In SPB (section 2.5), the molecular state is transferred into one of the $|J=1,m_J=\pm 1\rangle$ states before proceeding to the interaction region (section 2.6). Here, using NMR with the SOF technique, we transform the frequency shift between Tl spin up and down states, due to \mathcal{H}_{CPV} (equation (3)), into a population difference between these states. Subsequently, in SPC (section 2.7), one of the Tl spin state populations is transferred to a J=2 state. This makes the two populations resolvable with laser-driven transitions, to facilitate state readout (section 2.8). Finally, in the detection region, optical cycling and fluorescence collection are used for efficient, quasi-simultaneous detection of the two populations. The red, gray, and black curves in the figure indicate the magnitude of the electric field along, respectively, the beam direction Z, the interaction region field direction z, and the transverse electric quadrupole field directions X, Y.

the molecular beam. Here, laser-induced fluorescence (LIF) was recorded with a photomultiplier tube (PMT). The LIF signal as a function of laser detuning, with laser beams perpendicular to or at 45° to the TIF beam, yielded information on the velocity distributions. The longitudinal distribution is very nearly Gaussian, with mean $\langle v_Z \rangle = 184(17) \text{ m s}^{-1}$ and Gaussian width $\sigma_{v_Z} = 16.1(8) \text{ m s}^{-1}$. The latter corresponds to translational temperature $T_{\rm tr} = 7.0(7)$ K. The TIF beam divergence was determined from the shape of an isolated *Q*-branch ($\tilde{J}' = J$) absorption line, probed upstream of any collimation. The FWHM spread in transverse velocity here was 93(3) m s⁻¹, corresponding to a divergence cone half-angle of $14.0(1.5)^{\circ}$.

The rotational temperature was determined by measuring the population in different rotational states via the size of LIF signals on R-branch transitions, where $\widetilde{J}' = J + 1$. The laser can resolve hyperfine structure in the excited but not in the ground state. Targeting the excited-state sublevel with the largest possible angular momentum, $\widetilde{F}' = \widetilde{J}' + 1 = J + 2$, ensures that only a single ground state hyperfine sublevel, with F = J + 1, is excited. This considerably simplifies the extraction of rotational level

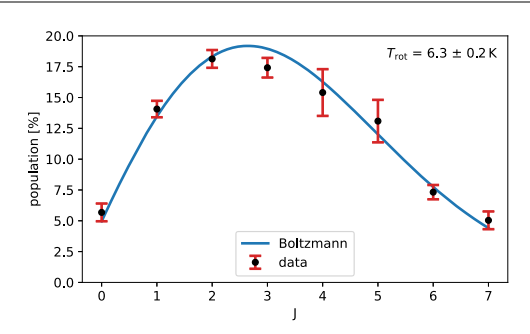


Figure 7. Relative rotational state populations of TIF in the CeNTREX beam source with typical conditions as described in the text, overlaid with a fit to a Boltzmann distribution. From the fit, we find the rotational temperature $T_{\rm rot} = 6.3(2)$ K.

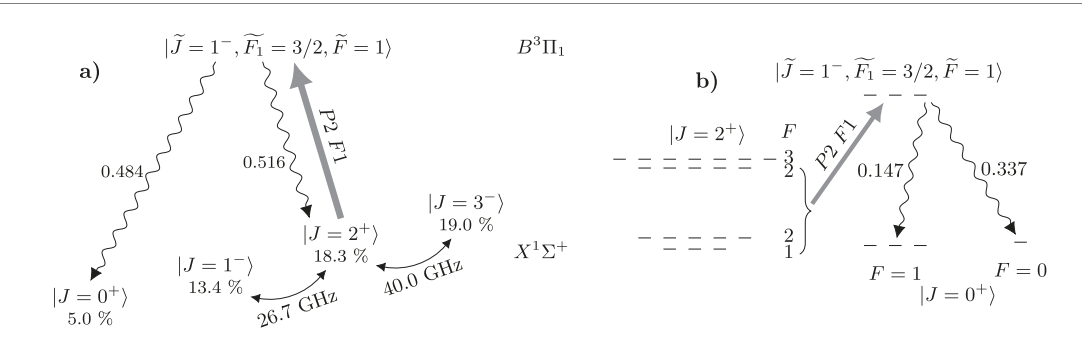


Figure 8. Rotational cooling scheme. (a) The thick solid arrow marks a UV laser driving the P2F1 transition; bent arrows represent microwaves, and wavy arrows indicate spontaneous emission. Rotational branching ratios are calculated with data from [37]. The odd-parity $\tilde{J}' = 1^-$ excited state can only decay to states with $J = 0^+, 2^+$. Percentages under the ground-state kets are the thermal population at temperature $T_{\rm rot} = 6.3$ K, prior to rotational cooling. (b) Hyperfine structure relevant to optical pumping. Decays back to $J = 2^+$ are not shown. The P2F1 transition does not excite $|J = 2^+, F = 3\rangle$. The nearest optical transition that couples to the $J = 2^+$ hyperfine manifold is separated from this line by about 550 MHz.

populations from LIF signals. Subsequently, the relative populations are fit to a Boltzmann distribution,

$$P(J) = g(J) \exp\left(-\frac{BJ(J+1)}{k_{\rm B}T_{\rm rot}}\right),\tag{8}$$

where g(J) = 4(2J + 1) is the degeneracy of each rotational level. This procedure, illustrated in figure 7, yielded $T_{\text{rot}} = 6.3(2)$ K.

From known line strengths [37, 38, 43], calculated solid angle of fluorescence detection, and calibrated PMT sensitivity, we found a time-averaged TIF beam intensity of 5×10^{12} molecules/state/sr/s. Here, each m_F sublevel is considered one state, and the time average is taken over 1 s when operating at 50 Hz pulse repetition rate. This is comparable to intensities found in other cryogenic buffer gas beam sources [42].

2.2. Rotational cooling

In a Boltzmann distribution at $T_{\rm rot}=6.3$ K, about 50% of the TIF population is in states with J=0 through J=3. To maximize the Schiff moment measurement sensitivity in CeNTREX this population is dissipatively pumped to the J=0, F=0 level, which becomes the initial state for all further steps in the experiment. This rotational cooling will be accomplished using a single optical pumping laser and two microwave driving fields. The laser couples the J=2 state to an excited state with $\widetilde{J}'=1$. We calculate that about half of the decays from the excited $\widetilde{J}'=1$ state end in the J=0 state; nearly all of the remainder returns to the J=2 state. Branching to other vibrational states is $\lesssim 1\%$ [37, 39]. The microwaves resonantly couple $J=1 \leftrightarrow 2$ and $J=2 \leftrightarrow 3$. Repeated excitation-decay cycles then lead to accumulation of population from J=1,2, and 3 into the J=0 state, as shown in figure 8.

The presence of hyperfine structure adds considerable complexity to rotational cooling in TIF. The aim is to accumulate population in the J=0, F=0 hyperfine level. While the ground-state hyperfine splitting is smaller than the laser linewidth, the excited-state hyperfine levels are well separated. We tune the J=2 optical pumping laser to resonance with the $\widetilde{J}'=1, \widetilde{F}_1'=3/2, \widetilde{F}'=1$ level. We refer to this line as the P2F1 transition. (As usual, this P-branch transition has $\widetilde{J}'=J-1$.) Without a considerable effort, this level structure will only support an extremely low excitation and pumping rate due to the formation of long-lived coherent dark states [44] within the manifold of unresolved ground-state hyperfine and Zeeman

sublevels. In CeNTREX, these dark states will be rapidly destabilized [44] by switching the polarizations of the laser and both microwave beams [45, 46], and ensuring that no pair of the three beams are either parallel or perpendicular to each other¹¹. Even with these measures, the excitation rate on the laser-driven transition is bounded by $\Gamma_{\rm sc} \lesssim \gamma_B \cdot n_{\rm e}/(n_{\rm g}+n_{\rm e})$ [47], where $n_{\rm e}=3$ is the number of excited state sublevels, $n_{\rm g}=60$ is the number of simultaneously coupled ground-state sublevels, and $\gamma_B\approx \times 1.6$ MHz.

We have performed numerical simulations to estimate the efficiency of this rotational cooling scheme, by solving the optical Bloch equations for the full 67-level system coupled by microwaves, lasers, and spontaneous emission. Our simulations include a realistic transverse velocity distribution; from trajectory simulations, we find that the Doppler shifts experienced by molecules that can enter the lens are as large as $\pm 14\gamma_B$. This range is difficult to saturate with simple power broadening, given the limited laser power available in the UV. To use this power most effectively, we add many sidebands to broaden the laser frequency such that it roughly matches the full Doppler width. In the simulations, we phase-modulate the laser (with its carrier frequency set to resonance with zero-velocity molecules) at frequency $f_{\rm mod} = \gamma_B = 1.6$ MHz and with modulation depth $\beta_{\rm mod} = 8.5$. (These parameters can be reached with a commercial electro-optic modulator.) We assume a realistic laser intensity (~ 6 mW mm⁻²) in a beam multi-passed across the molecular beam to achieve total interaction length of ~ 1 cm (corresponding to 50 μ s interaction time), and 100 mW of microwave power in 2.5 cm diam. beams at each frequency.

Under these conditions, we find that 78% of all molecules originally in the J=0-3 states are accumulated into sublevels of the J=0 state. Of these, $\sim 50\%$ are in the desired $\left|J=0,F_1=\frac{1}{2},F=0,M_F=0\right\rangle$ hyperfine state. This corresponds to a 24-fold increase compared to the initial thermal population in this state, due to rotational cooling. Based on results from simulations under other conditions, and recent demonstrations of extended multipass geometries [48], we believe that nearly complete pumping can be achieved by extending the interaction length to 5 cm. This could increase the desired state population by another factor of 1.28, and also dramatically reduce residual populations in excited rotational levels (which can contribute to background signals and/or systematic errors). Both experimental and further numerical tests of the rotational cooling are ongoing.

2.3. State preparation region A

The EQL in CeNTREX is designed to focus molecules in the $|J=2, m_J=0\rangle$ state (see section 2.4). After rotational cooling, a majority of the population is in the state $|J=0, F=0\rangle$, which is a pure $I_t=0$ (singlet) state of the nuclear spins. In SPA, the population of this state is coherently transferred to a $|J=2, m_J=0\rangle$ state using a two-stage AP protocol. In each stage, J increases by one and m_J is unchanged, while (nominally) $I_t=0$ throughout.

The driving field is provided by two CW, single-frequency free-space microwave beams, tuned to near resonance with the $J=0 \rightarrow J=1$ and $J=1 \rightarrow J=2$ transitions. The beams are produced by spot-focusing horns, spatially offset so the beam profiles have no significant overlap. The time-varying detuning of each beam from its respective resonance is provided by the quadratic Stark shift due to a spatially varying DC electric field as the molecules fly through the region. The desired $\Delta m_J = \Delta I_{\rm t} = 0$ transitions are selectively driven by π -polarized microwaves. Due to geometric constraints, this requires the DC electric field, \mathcal{E} , to lie along the molecular beamline, \hat{Z} . Figure 6 has a schematic overview of this region.

For efficient population transfer via AP, the adiabaticity condition must be fulfilled [49]:

$$\frac{\mathrm{d}\Delta}{\mathrm{d}t} \ll \Delta^2 + \Omega_{\mu\mathrm{w}}^2,\tag{9}$$

where Δ is the detuning and $\Omega_{\mu w}$ the Rabi rate of the microwave drive. Furthermore, the detuning at large times before and after the AP interaction must be larger than the microwave Rabi rate. This is accomplished with fields as shown in figure 9. We simulated the TIF state evolution in the SPA region with peak Rabi rates $\Omega_{\mu w}=70$ kHz, perfectly pure π -polarization, microwave intensity profile as measured from the focusing horns, \mathcal{E}_Z field from finite element calculations, and including the effect of the Earth's magnetic field. With these assumptions, we found a state transfer efficiency of 99%.

We are confident that high transfer efficiency can also be reached in the real experiment. AP is a threshold process in that as long as the adiabaticity condition is fulfilled, the state transfer occurs with an efficiency close to 100% [49]. By making sure that the adiabaticity condition is satisfied with a sufficiently safe margin, the effects of various factors that might be expected to lower the efficiency can be mitigated. We have simulated the effect of numerous realistic imperfections such as spatial inhomogeneity of the

¹¹ Due to the selection rule ($\Delta F = 0, \pm 1$), the (J = 2, F = 3) state is dark with respect to laser excitation in this scheme. However, even the population in this state can eventually be optically pumped, since the strong $J = 2 \leftrightarrow J = 3$ microwave field couples this state to the J = 2, F = 2, 2, 1 states via Raman-type transitions.

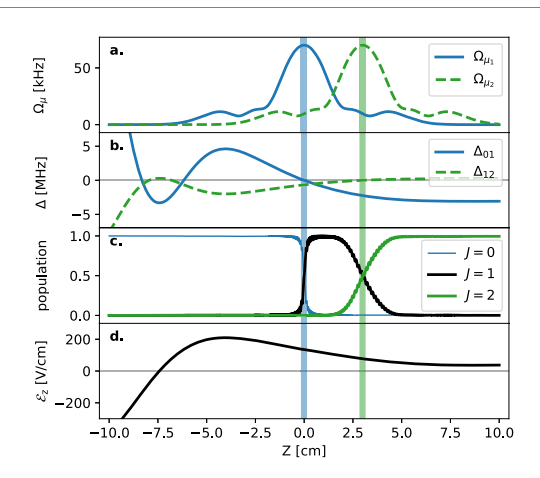


Figure 9. Rabi rates, detunings, state populations and field amplitudes versus position in SPA, where \hat{Z} is the molecular beam direction. (a) Calculated Rabi rates $\Omega(Z)$, based on the measured intensity profile from the spot-focusing horns. (b) Stark-shifted detunings Δ_{01} and Δ_{12} of the transitions $J=0 \leftrightarrow 1$ and $J=1 \leftrightarrow 2$, respectively. (c) Calculated populations of relevant states as the molecules travel through the SPA region, showing a simulated transfer efficiency from J=0 to J=2 of 99%. (d) Electric field \mathcal{E}_Z , based on finite element simulations.

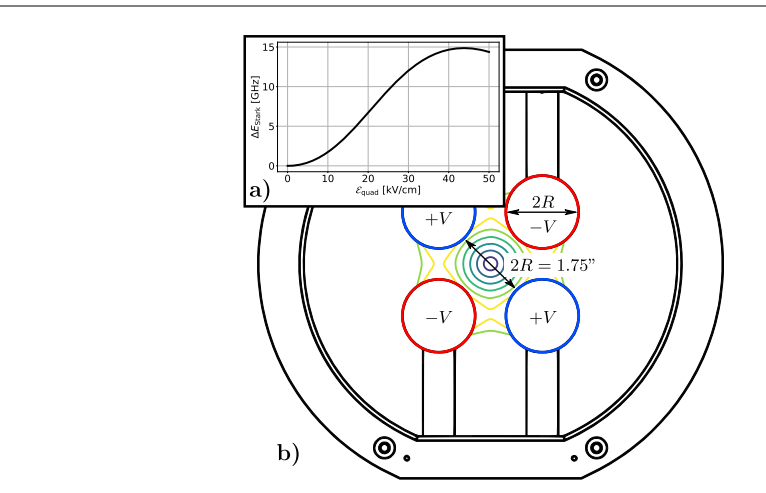


Figure 10. (a) Stark shift of the J=2, $m_I=0$ hyperfine manifold of states. (b) Front view of the EQL. Colored curves are equipotential surfaces. The electrodes have length l=60 cm, and applied potentials $\pm V$ up to ± 30 kV. The electrode support structure is mounted on translation stages (not shown) that allow for alignment of the lens under vacuum.

microwaves and the \mathcal{E} -field, Doppler shifts, and microwave polarization misalignment; we find that with the available microwave intensity, the efficiency is not noticeably degraded in simulations.

2.4. Electrostatic quadrupole lens

The molecular beam exiting the source is spread over a wide solid angle, so the beam intensity decreases as the square of the distance from the source. The total distance from beam source to final detection in CeNTREX is ≈ 6.4 m, so beam focusing can substantially improve the signal strength. To accomplish this, an EQL will be employed.

An EQL with four equidistant cylindrical electrode rods, held at alternating positive and negative potentials of the same magnitude *V*, generates an electric quadrupole field of magnitude

$$\left|\mathcal{E}_{\text{quad}}(r)\right| = \frac{2Vr}{R^2},\tag{10}$$

where 2R is both the bore diameter of the lens and the electrode diameter, and r is the distance from the central axis of the quadrupole. A front view of the lens is shown in figure 10(b). The J=2, $m_J=0$ states in TIF have a quadratic Stark shift in fields up to $\mathcal{E}\approx 20$ kV cm⁻¹, and slightly slower than quadratic to ~ 30 kV cm⁻¹ (figure 10(a)). For electrode potentials of $\pm V=\pm 30$ kV, the fields inside the bore of the lens do not exceed 30 kV cm; hence, most molecules in the lens bore remain in the quadratic Stark shift regime.

A quadrupole field acting on molecules with a quadratic Stark shift produces a harmonic potential along the radial direction within the lens. Under these conditions, the electrostatic lens acts as an analogue to a

thick optical lens [50]: the lens can be thought of as imaging the molecular beam from the source to the detection region. The trajectories of the molecules can be described by the ray transfer matrices of a thick optical lens [51, 52]:

$$\begin{pmatrix} r_{i} \\ \dot{r}_{i}/v_{Z} \end{pmatrix} =$$

$$\begin{pmatrix} 1 & z'_{i} \\ 0 & 1 \end{pmatrix} \begin{pmatrix} 1 & 0 \\ -f^{-1} & 1 \end{pmatrix} \begin{pmatrix} 1 & z'_{o} \\ 0 & 1 \end{pmatrix} \begin{pmatrix} r_{o} \\ \dot{r}_{o}/v_{Z} \end{pmatrix},$$
(11)

where $r_{o/i}$ is the radial position of the molecule in the object/image plane (in our case beam source/detection region), $z'_{o,i}$ is the distance from the object/image plane to the entrance/exit principal plane of the lens, v_Z is the molecular velocity component along the beam direction (i.e. longitudinal velocity), and f is the effective focal length given by

$$f = \frac{1}{p \sin(pl)}, \quad p = \left(\frac{8CV^2}{R^4 m v_Z^2}\right)^{1/2}.$$
 (12)

Here, l is the length of the quadrupole lens, m the molecular mass, and C is a constant corresponding to the strength of the quadratic Stark shift for a given J, m_I state [36]:

$$C = \frac{\mu_e^2}{2hB} \frac{J(J+1) - 3m_J^2}{J(J+1)(2J-1)(2J+3)},$$
(13)

where B is the rotational constant (table 1) and μ_e the molecular EDM. As shown in equation (12), the focal length depends on the velocity of the molecules. The spread of longitudinal velocities in the molecular pulse thus gives a range of focal lengths; this chromatic aberration increases the focal spot size. Aberrations due to deviation of the Stark shift from a purely quadratic spatial dependence have a similar effect.

Due to the complexity added by the aberrations, the length and bore diameter of the lens were optimized with Monte Carlo simulations of molecular trajectories through the entire apparatus. These simulations were done before much of the beamline was designed and prior to measurements of the molecular beam properties, and thus educated guesses had to be made for the parameters. For the molecular beam we assumed a Gaussian longitudinal velocity distribution with $\langle v_Z \rangle = 200 \text{ m s}^{-1}$ and $\sigma_{v_Z} = 13 \text{ m s}^{-1}$. The beamline was taken to have a distance of 0.81 m from the molecular source to the start of the lens, and 3.63 m from the end of the lens to detection. The detection region was taken to have an acceptance area of 10 mm \times 30 mm. The source was taken to have a diameter of 20 mm, and was located 0.25' downstream from the cold cell exit aperture. This was based on an estimate of the molecular cloud size at the 'zone of freezing' where interactions between molecules are assumed to have ceased [42]. The length and diameter of the lens were then optimized by maximizing the expected number of detected molecules when the electrodes were at \pm 30 kV. The optimal combination was found to be a diameter 2R = 1.75'', and a length l = 60 cm. The simulated gain in the number of molecules making it to detection was a factor of 24.

Some of the beamline and molecular beam properties are now known better than when the lens was designed. The measured molecular beam velocity is slightly lower at $\langle v_z \rangle = 184$ m s⁻¹ (section 2.1) than previously assumed. To compensate for the lower velocity, the electrode voltages are lowered to ± 27 kV. The source-to-lens-distance is 1.01 m, and the lens-to-detection-distance 4.45 m (liable to change by ~ 10 cm as the SPB and SPC regions are designed). With these parameters, the simulated gain in the number of molecules reaching the detection region is a factor of 23.2 \pm 0.9 where the uncertainty is based on Poisson statistics in the simulation.

2.5. State preparation region B

After the electrostatic lens, TIF resides in a J=2, $m_J=0$ state, but the NSM measurement requires molecules to be in a J=1 state with $m_J=\pm 1$ [32, 53] (see section 1.2). The required state transfer takes place in SPB. To achieve this, a resonant microwave field with x-polarization (in 'interaction region' coordinates) will be applied in the presence of a magnetic field, $\mathcal{B}_{\text{SPB}}\approx 10$ G, and a quantizing electric field, $\mathcal{E}_{\text{SPB}}\approx 50$ V cm⁻¹. The \mathcal{B}_{SPB} -field is parallel to $\mathcal{E}_{\text{SPB}}=\mathcal{E}_{\text{SPB}}\hat{z}$, and acts to distinguish $\pm m_J$ states. Here, AP can drive undesired transitions to unwanted states nearby in energy. So, here we use a microwave π -pulse to achieve optimized transfer efficiency. With a peak Rabi rate $\Omega_{\mu w}=1.5$ kHz, the simulated transfer efficiency is $\sim 96\%$. In practice, the transfer efficiency is likely to be reduced due to non-uniformities of the electric and magnetic fields, since changes in the fields cause the transition frequencies to shift away from the microwave frequency. To achieve the quoted 96% efficiency, \mathcal{B} needs to be uniform to within $\delta \mathcal{B}/\mathcal{B} < 10^{-3}$ and \mathcal{E} to within $\delta \mathcal{E}/\mathcal{E} < 10^{-4}$. We are designing coils and electrodes to meet these specifications.

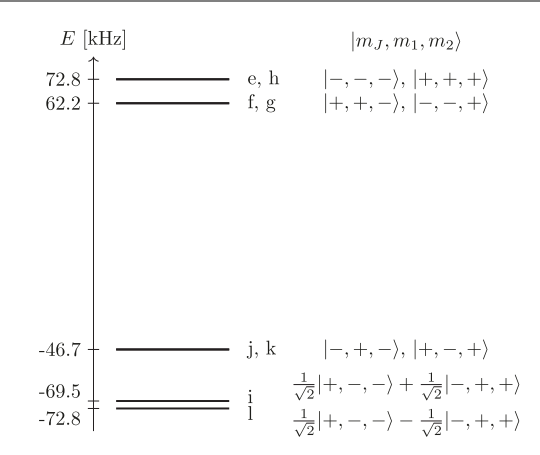


Figure 11. Hyperfine level structure of TIF $|J=1, m_J=\pm 1\rangle$ states in $\mathcal{E}=30 \text{ kV cm}^{-1}$ and $\mathcal{B}=0$, as will be present in the MI region. Lettered naming labels correspond to those in [32]. For brevity, only the sign of the quantum numbers is shown; the full values are $m_J=\pm 1$, $m_1=\pm 1/2$, $m_2=\pm 1/2$, where $m_1(m_2)$ is the TI (F) nuclear spin. The zero of energy is arbitrary.

2.6. Main interaction region

In order to measure the Schiff moment, a large, uniform external electric field ($\mathcal{E}_{\text{MI}} = 30 \text{ kV cm}^{-1}$, along \hat{z}) polarizes the molecules. In this large field, energies of the $\tilde{J} = 1$, $m_J = \pm 1$ manifold of hyperfine states are close, relative to their splittings to all other \tilde{J} , m_J states. The states within the $\tilde{J} = 1$, $m_J = \pm 1$ subspace are then well-described [30] by the effective Hamiltonian¹²

$$\mathcal{H}_{\text{eff}} = -\mu_{J} J_{z} \mathcal{B}_{z} + (-\mu_{1} \mathbf{I}_{1} - \mu_{2} \mathbf{I}_{2}) \cdot \mathcal{B}$$

$$-\mu_{1} I_{1z} J_{z} \mathcal{B}_{1}^{\text{int}} - \mu_{2} I_{2z} J_{z} \mathcal{B}_{2}^{\text{int}} + C_{s} I_{1z} I_{2z}$$

$$+ C_{t} (J_{+}^{2} I_{-,1} I_{-,2} + \text{h.c.}) + W_{S} S \frac{\mathbf{I}_{1}}{I_{1}} \cdot \hat{\mathbf{n}}.$$
(14)

Here, \mathcal{B}^{int} denotes an effective intra-molecular magnetic field along $\langle J \rangle$ that arises from the spin–rotation terms in equation (7), while C_s and C_t are effective scalar and tensor spin–spin interactions, respectively, that arise from the spin–spin terms in equation (7). The subscripts z, +, – on operators refer to the usual angular momentum projection, raising, and lowering operators, respectively.

The degree of electric polarization, \mathcal{P} , is given by

$$\mathcal{P} = \langle \hat{\mathbf{n}} \cdot \hat{\mathcal{E}} \rangle = \langle \cos \theta \rangle, \tag{15}$$

where θ is the angle between \hat{n} and \mathcal{E}_{MI} . For a state in the $J=1, m_J=\pm 1$ manifold at $\mathcal{E}_{\text{MI}}=30$ kV cm⁻¹, $\mathcal{P}=0.547$. To determine the ²⁰⁵Tl NSM, we measure how the energy splitting between two states with the same m_J values but opposite Tl spin projections ($m_1=\pm 1/2$) changes, when \mathcal{E}_{MI} is reversed. As discussed in section 1, when S is non-zero this splitting will shift by $\pm 2\Delta_{\text{CPV}}=\pm 2W_S\mathcal{P}$ sgn(\mathcal{E}_{MI}) (figure 1). The states in the $J=1, m_J=\pm 1$ manifold in the electric field of magnitude \mathcal{E}_{MI} are shown in figure 11; the pairs that flip only the Tl spin \mathbf{I}_1 are j/e and k/h, both with a separation of 119.517 kHz due mainly to the effective internal magnetic field and the scalar spin–spin interaction. Hence, we seek to measure the splittings between these levels, and how they change when \mathcal{E} or other experimental parameters are reversed.

The energy splitting is measured with a classic SOF technique for nuclear magnetic resonance [40, 41], albeit with the external \mathcal{B} -field set to zero. The RF drive frequency is set to resonance with the j/e or k/h transition, i.e. $\hbar\omega_{\rm RF}\approx\mu_{\rm Tl}\mathcal{B}_{\rm int}-C_{\rm s}/2$. The first RF pulse in the SOF sequence creates a superposition of the Tl spin-up and spin-down states; e.g. starting in state e, the $\pi/2$ pulse creates a superposition between states e and j. Then, during a period T of free precession, the accumulated phase between the up (e or h) and

The effective Hamiltonian formulation (see, e.g. reference [36]) is useful to describe states in a near-degenerate subspace that couple only weakly to all other states in a larger Hilbert space. We split the Hamiltonian of equation (7) into a large 0th-order term, $\mathcal{H}^{(0)} = \mathcal{H}_{\text{rot}} + \mathcal{H}_{\text{s}}$, and a small 1st order term, $\mathcal{H}^{(1)} = \mathcal{H}_Z + \mathcal{H}_{\text{sr}} + \mathcal{H}_{\text{ss}}$. We then compute eigenstates of $\mathcal{H}^{(0)}$, operating on the full Hilbert space of all spin-rotation levels, and use the set of all $\widetilde{J} = 1$, $m_J = \pm 1$ states as (degenerate) basis states for the subspace. To lowest order, the effective Hamiltonian \mathcal{H}_{eff} acting on this subspace consists only of the terms in $\mathcal{H}^{(1)}$ that couple states within the subspace (including diagonal terms). That is, \mathcal{H}_{eff} is derived by first discarding all operator terms in the full Hamiltonian of equation (7) that change m_J by ± 1 unit, and hence only connect states in the subspace to distant outside states, then computing matrix elements of the remaining operators between the basis states. The resulting coefficients C_s and C_t are linear combinations of c_3 and c_4 , but, because J is not a good quantum number, simple analytic expressions cannot be given for their weights.

down (j or k) states is

$$\phi \approx \left(-\mu_{\text{Tl}}\mathcal{B}_{\text{int}} \operatorname{sgn}(m_J) + C_s m_{I_2} + 2W_S S \mathcal{P} \operatorname{sgn}(\mathcal{E}_{\text{MI}})\right) T/\hbar.$$
(16)

The second RF pulse maps ϕ onto the relative population in the spin-up and spin-down states. The probability of a transition from spin-up to spin-down is [41]

$$P_{\uparrow \to \downarrow} = \sin^2 \frac{1}{2} \Omega_{\text{RF}} \tau \cos^2 \frac{1}{2} \left(\phi_{\text{CPV}} + \phi_{\text{SOF}} \right), \tag{17}$$

where $\phi_{\rm SOF}$ is the phase offset between the first and second RF pulses, $\Omega_{\rm RF}$ is the Rabi frequency of the RF magnetic field, τ is the time spent in the perturbing RF field, and

$$\phi_{\text{CPV}} = 2W_{\text{S}}SP \operatorname{sgn}(\mathcal{E}_{\text{MI}})T/\hbar = 2\Delta_{\text{CPV}}T/\hbar. \tag{18}$$

The aim is to determine ϕ_{CPV} ; from its measured value and the known value of T, Δ_{CPV} can be found. The phase difference ϕ_{SOF} will be set to have magnitude $\pi/2$ and to alternate in sign: $\phi_{\text{SOF}} = \pm \pi/2$. This yields maximal sensitivity to the small energy shift Δ_{CPV} .

In a zero magnetic field environment with $\mathcal{E}_{\mathrm{MI}}$ present, ϕ_{CPV} only accumulates due to the T-violating frequency shift. In practice, magnetic fields cannot be fully eliminated from the interaction region, and will generate additional frequency shifts. To minimize the contribution of magnetic fields, we will construct a magnetic shield consisting of several concentric cylinders. Currently, a four-cylinder shield, with 12 layers of Metglas high-permeability material [54] on each cylinder, is planned. These will be augmented with shim coils inside and outside the shields for additional magnetic field control. We aim to achieve sub-10 μ G residual fields (see section 3.3).

The externally applied electric field \mathcal{E}_{MI} will be generated with two quartz electrodes of 3 m length, separated by 2 cm, with a Rogowski profile [55, 56] to prevent formation of large edge fields. The electrodes will be coated with a conductive water-based colloidal graphite coating. The choice of coated quartz electrodes was made to minimize electrical conductance that leads to magnetic Johnson noise [57–59]. To further minimize Johnson noise, the vacuum chamber surrounding the MI region will be constructed from a quartz tube (3.5 m long, 26 cm O.D., 2 cm wall thickness). To prevent charge buildup, the inner surface of the tube will be grounded with either a thin conducting sheet or a conductive coating.

Coils to produce the SOF NMR fields will be placed outside the vacuum chamber, placed symmetrically about the center of the electrodes and separated by distance $L_{\text{SOF}} \approx 2.5$ m. Several additional coils will be mounted to allow application of small DC $\boldsymbol{\mathcal{B}}$ -fields and gradients in various directions; these will be used mostly for diagnosing and correcting systematic errors.

2.7. State preparation region C

After the MI region, molecules populate two states, $|J=1,m_I,m_{I_1}=+1/2,m_{I_2}\rangle$ and $|J=1,m_J,m_{I_1}=-1/2,m_{I_2}\rangle$, which cannot be distinguished optically. To enable optical detection, population from one or both of these states will be transferred to different rotational states, which are spectrally resolvable by a probing laser. This will allow optical detection of each original spin-state population (section 2.8). An optimized scheme for this state transfer mechanism is currently being investigated, but will likely involve a microwave π -pulse, mirroring SPB.

2.8. Fluorescence detection region

Detecting the populations in the two rotational states resulting from state transfer region C, which carry the information about the accumulated phase ϕ , will be achieved with optical cycling to maximize the number of emitted photons from each molecule. This cycling, which has been demonstrated experimentally in TIF [48], will allow for near unit-efficiency detection of each molecule.

The rotational sublevels of the TIF ground state $X^1\Sigma^+$ are far enough apart to require two detection lasers. Rapid switching between the lasers will allow for quasi-simultaneous readout of both the spin-up and spin-down populations in a single molecular-beam pulse, minimizing the effect of molecule number fluctuations within and between pulses [60]. The switching, to be accomplished with acousto-optic modulators, will allow enough dead time between switches for the excited state to decay, but also will be rapid enough such that each molecule sees both laser frequencies multiple times while traveling through the optical interaction region. A similar scheme is implemented by the ACME experiment [61].

The resulting fluorescence will be collected by a combination of high numerical aperture lenses and mirrors to cover a total solid angle of $\approx 0.3 \times 4\pi$ sr. With PMT quantum efficiency of $\approx 25\%$, each emitted photon will then be detected with $\approx 7.5\%$ efficiency. Hence, scattering $\gtrsim 30$ photons per molecule will be

sufficient that each molecule is detected with \gtrsim 90% probability. Based on known branching ratios for decay out of each cycling transition in TlF [37], this should be feasible.

The fluorescence signals S_{\uparrow} and S_{\downarrow} , corresponding to populations in the Tl spin-up and spin-down states after the SOF sequence, are then used to compute the asymmetry A, defined as:

$$\mathcal{A} \equiv \frac{S_{\uparrow} - S_{\downarrow}}{S_{\uparrow} + S_{\downarrow}}.\tag{19}$$

With the SOF drive frequency on resonance,

$$\mathcal{A} \approx 1 - 2\sin^2\Omega_{\rm RF}\tau\cos^2\frac{1}{2}\left(\phi_{\rm CPV} + \phi_{\rm SOF}\right). \tag{20}$$

For $\phi_{\rm SOF}=\pm\pi/2$ and $\Omega_{\rm RF}\tau=\pi/2$, this simplifies to $\mathcal{A}\approx\pm\sin\,\phi_{\rm CPV}\approx\pm\phi_{\rm CPV}$.

2.9. Laser and microwave systems

To accomplish the Schiff moment measurement in TIF, three UV lasers at 272 nm are required: one for rotational cooling, and two for the quasi-simultaneous state readout.

Three IR seed lasers are frequency doubled twice to reach UV. The IR seeds are tunable fiber lasers, providing ~ 10 mW per laser at 1087 nm. All of the seed beams are amplified with Yb fiber amplifiers, then doubled into green (544 nm). Two of the systems accomplish this by coupling their amplified output (1.4 W) to a home-built resonant cavity containing a PPKTP crystal, delivering ~ 500 mW of green light in free space. A third system uses a high-power amplifier and a single-pass doubler to produce 1.4 W of green light from a single-mode fiber. For all systems, the green light is coupled into a commercial resonant cavity containing a BBO crystal. This frequency-doubles the green light to produce $\lesssim 80$ mW of 272 nm single frequency, tunable light from each system.

These UV lasers are locked to a tunable offset from resonance, using a frequency transfer scheme employing scanning confocal cavities and a single stable reference laser [62–65]. For the reference laser, we tightly lock a tunable external-cavity diode laser to a D_2 transition in atomic Cs, using modulation transfer spectroscopy (MTS) [66], to achieve absolute frequency stability of better than 100 kHz.

Several microwave-frequency \mathcal{E} -fields are required to couple the rotational ground states in the state preparation regions. To control the spatial distribution of these microwave fields, we use microwave quasi-optical spot-focusing horns that create nominally Gaussian, traveling-wave beams, with their waists centered on the molecular beam. The microwave beams enter and exit the vacuum chamber through windows large enough to ensure negligible clipping of the intensity profile. These windows have a thickness $\lambda/2$ that, much like an anti-reflection coating for optical windows, causes destructive interference between reflections off the front and back surfaces of each window. Furthermore, each beam, on exiting the chamber, is received by a horn identical to the transmitting horn, at the same distance from the waist. Hence, the microwave beam is nominally matched in spatial mode to the receiving horn, which is terminated in 50 Ohms to absorb the incident power. These measures minimize the reflected intensity, to prevent unwanted standing wave components. Each horn is fed through an orthomode transducer; switches after the microwave generators and amplifiers can direct the full power to either input port, and hence deliver either allowed linear polarization to the molecules.

2.10. State evolution between regions

The different functional regions of CeNTREX require \mathcal{E} - and \mathcal{B} -fields of widely varying magnitude and orientation. Hence, in the spaces between the functional regions, spatially-varying fields will be present. These manifest as time-varying fields in the molecules' rest frame, resulting in unwanted transfer of molecular population from the desired state to undesired states. This loss reduces statistical sensitivity and can lead to systematic errors. For example, if molecular population is lost non-uniformly over the cross section of the molecular beam, an inhomogeneous distribution of molecules will result. When combined with spatial field gradients within the MI region, this has been observed to cause systematic errors in related experiments [61]. Understanding how the relevant quantum states evolve when molecules travel between functional regions is therefore important both in terms of optimizing the statistics and avoiding systematic errors in CeNTREX.

We have performed extensive numerical simulations to identify optimized schemes for transfer between regions in CeNTREX, and to understand how undesired states can be populated here. We find it should be possible to achieve near 100% efficiency in all cases. Because the between-region state evolution in CeNTREX is non-trivial to understand, yet appears to be sufficiently under control, we do not discuss it in detail here. Interested readers can find a thorough treatment in appendix A.

3. Sensitivity and systematics

3.1. Anticipated sensitivity

The molecule-shot-noise limited (SNL) sensitivity for an SOF frequency measurement in a beam is given by

$$\delta\nu_{\rm SNL} = \frac{1}{2\pi T} \frac{1}{C_{\rm SOF}} \frac{1}{\sqrt{N_{\rm d}N_{\rm p}}} Z. \tag{21}$$

Here T is the total interaction time in the MI region, $L_{SOF}/\langle v_z \rangle$, C_{SOF} is the SOF fringe contrast, N_d is the number of molecules detected per beam pulse, and N_p is the number of pulses used in the measurement. CeNTREX is expected to achieve $C_{SOF} \approx 1$, as in the ACME electron EDM measurement that uses a similar detection scheme [61]. The factor Z, which takes values $1 < Z < \sqrt{2}$, accounts for excess noise that can arise when detecting fluorescence from a partially-closed cycling transition [67]. To be conservative, we take $Z = \sqrt{2}$.

We estimate $N_{\rm d}$ as follows. The measured time-averaged beam intensity is 5×10^{12} molecules/state/sr/s (section 2.1), corresponding to 1×10^{11} molecules/state/sr/pulse. Rotational cooling results in a simulated 24-fold increase in the number of molecules in the desired F=0, $m_F=0$ state (section 2.2). Combining the simulated state transfer efficiencies of SPA (99%), SPB (96%), and SPC (96%) (sections 2.3, 2.5 and 2.7), giving a cumulative transfer efficiency of $\approx 91\%$. Given the distance of the FD region from the source and its transverse area $18 \text{ mm} \times 30 \text{ mm}$, the solid angle subtended by the FD region is 1.3×10^{-5} sr. From simulations of the EQL (section 2.4), the gain in signal from energizing the lens should be 24. Combining these with the anticipated detection efficiency of 90%, we expect $N_{\rm d} \approx 6.1 \times 10^8$ molecules/pulse to be detected in the FD region.

Combined with $\langle v_z \rangle = 184 \text{ m s}^{-1}$ and $L_{SOF} \approx 2.5 \text{ m}$, we estimate a shot noise-limited frequency shift sensitivity of

$$\delta \nu_{\rm SNL} pprox \frac{0.7}{\sqrt{N_{\rm p}}} \, \, {\rm mHz}.$$
 (22)

With a total measurement time of 300 h and a 50 Hz repetition rate, corresponding to $N_{\rm p}\approx 5.4\times 10^7$, the final sensitivity is projected to be $\delta\nu_{\rm SNL}\approx 90$ nHz. Recalling that the CPV energy shift is $2\Delta_{\rm CPV}$, this is equivalent to $\delta\Delta_{\rm CPV}\approx 45$ nHz. For comparison, the previous best limit achieved $\delta\Delta_{\rm CPV}\approx 120~\mu{\rm Hz}$ [30]. Hence we anticipate that CeNTREX can achieve a 2500-fold statistical improvement over the CPV limits given in equation (6).

3.2. Extracting Δ_{CPV}

We will extract the CPV energy shift Δ_{CPV} from our data using schemes similar to those used in prior experiments [32, 52, 61, 68] and described briefly here.

Recall that under ideal conditions, the signal asymmetry is given by $\mathcal{A} = \operatorname{sgn}(\phi_{\text{SOF}}) \sin \phi_{\text{CPV}}$. In practice, various experimental imperfections (e.g. deviations from exact RF phase and/or resonance frequency) generate an additional accumulated phase ϕ' during free precession in the interaction region. This modifies the asymmetry, such that $\mathcal{A} = \operatorname{sgn}(\phi_{\text{SOF}}) \sin(\phi_{\text{CPV}} + \phi')$. To isolate the CPV phase term, we measure \mathcal{A} under two different conditions where the sign of Δ_{CPV} reverses. This is the case, for example, when the direction of $\boldsymbol{\mathcal{E}}_{\text{MI}}$ is reversed. Then we calculate

$$A_{+\mathcal{E}_{\text{MI}}} - A_{-\mathcal{E}_{\text{MI}}} \approx \pm 2\phi_{\text{CPV}},$$
 (23)

independent of ϕ' so long as $\phi' \ll 1$. We refer to the reversal of \mathcal{E}_{MI} as E-modulation, and assign the parameter $E = \pm 1 = \text{sgn}\left(\mathcal{E}_{\text{MI}} \cdot \hat{z}\right)$.

It is possible to reverse the sign Δ_{CPV} in several other ways as well. For example, simultaneously reversing the magnetic fields in state preparation regions B and C, \mathcal{B}_{SPB} and \mathcal{B}_{SPC} , reverses the signs of all the angular momenta relative to the fixed laboratory z-axis. This corresponds to changing the signs of m_{I1} , m_{I2} , and m_{I3} , and hence also the sign of Δ_{CPV} . We refer to this reversal as B modulation and define $B = \text{sgn}(\mathcal{B}_{\text{SPB}} \cdot \hat{z})$. Finally, changing the frequency of the microwave fields in SPB and SPC makes it possible to select which states to initially populate for use in the MI region. For example, the transitions $e \leftrightarrow j$ and $h \leftrightarrow k$ are time-reversed versions of each other, meaning the effective internal magnetic field has opposite sign between them. This also changes the sign of Δ_{CPV} . We refer to this reversal as M modulation, and define $M = \pm 1$ corresponding to the $h \leftrightarrow k$ and $e \leftrightarrow j$ transitions, respectively.

While any of these modulations will, in principle, serve to isolate the contribution of ϕ_{CPV} , in practice we will employ all of them to provide various *in-situ* diagnostics. Our parameter naming convention here follows that of reference [30].

It proves useful to also employ a few more modulations. In particular, modulating the sign of the phase offset ϕ_{SOF} between the RF coils, as discussed in section 2.6, changes the sign of the asymmetry \mathcal{A} . This P modulation has no effect on Δ_{CPV} .

The fringe contrast C_{SOF} can be measured by alternatingly offsetting the SOF drive frequency from its resonance value ($f_0 = 119.516 \text{ kHz}$) by $\pm f_F$, where f_F is small compared to the SOF NMR linewidth. The quantity $\mathcal{A}_{+f_F} - \mathcal{A}_{-f_F}$ determines the slope of the resonance and hence C_{SOF} . This F modulation has no effect on Δ_{CPV} .

During the NSM measurement, all these modulation parameters will be frequently switched to determine Δ_{CPV} and to diagnose various possible contributions to ϕ' .

We denote the various combinations of asymmetries (i.e. phases) that can be constructed from these modulations with the notation $S_{p1,p2,...}$. Here, the subscripts denote a linear combination of phases odd under the listed modulation parameters p1, p2, ... and even under all other modulations. For example, the total phase shift ϕ_{CPV} is determined via

$$\phi_{\text{CPV}} \propto \mathcal{S}_{\text{PEBM}} = \sum_{i} (P_i E_i B_i M_i) \, \mathcal{A}_i,$$
 (24)

where P_i , E_i , B_i , and M_i are the signs of the modulation parameters during the *i*th dataset, and A_i is the measured asymmetry for that dataset. The quantity

$$S_{PF} = \sum_{i} (P_i F_i) A_i, \qquad (25)$$

which determines the slope of the frequency vs phase curve (and hence also the fringe contrast C_{SOF}), is used to convert ϕ_{CPV} to frequency units.

3.3. Known systematic errors

Here we discuss the anticipated magnitude of some known systematic errors in CeNTREX. Our discussion closely follows the notation and analysis of reference [30].

3.3.1. Imperfect \mathcal{E} -field reversal

The separation between the Tl spin up/down states in the J=1, $m_J=\pm 1$ manifold changes slightly when the externally applied \mathcal{E} -field changes in magnitude¹³. Any non-reversing contribution to \mathcal{E}_{MI} , e.g. from a stray DC field, thus leads to a frequency shift in the NMR transition that changes with the orientation of \mathcal{E}_{MI} . By brute-force diagonalization of the ground-state Hamiltonian of equation (7) with $\mathcal{E}=30$ kV cm⁻¹, the frequency shift can be calculated: see table 3. The pairs of states ej and hk that are used for the measurement both have an identical shift of -31.5 mHz (V/cm)⁻¹. Assuming the non-reversing \mathcal{E} -field component does not change significantly between subsequent M and B reversals, this effect will be suppressed in the quantity $\mathcal{S}_{\text{EBMP}} \propto \phi_{\text{CPV}}$ that is odd under both M and B. For the residual shift to be below our anticipated sensitivity, we will require a small non-reversing \mathcal{E} -field as well as accurate changes of both \mathcal{B} and the initial state of the NMR transition. The former quantity can be determined from the signal combination \mathcal{S}_{EP} , and then nulled by applying an appropriate offset voltage; the inaccuracy in latter two can be determined from $\mathcal{S}_{\text{EBMP}}$ when a deliberately large non-reversing \mathcal{E} -field is applied, then nulled if necessary.

3.3.2. Stray B-fields

The Centrex measurement will be performed with a nominally zero \mathcal{B} -field in the MI region. Significant effort will be made to minimize any residual stray fields, but nevertheless some will persist. These can arise, e.g. from leakage through, or residual magnetization of, the magnetic shielding. These stray \mathcal{B} -fields can lead to systematic errors via two mechanisms: direct shifts, and in combination with motional-field effects.

For the pair of states ej and hk, a \mathcal{B} -field along \mathcal{E}_{MI} (i.e. \mathcal{B}_z) generates a direct frequency shift of ± 2.5 mHz μG^{-1} , where the sign applies for the ej and hk transition, respectively. CeNTREX aims for sub-10 μG residual \mathcal{B} -fields, which will alone shift the transition frequency by $\mathcal{S}_{\text{B}} \approx \pm 25\,$ mHz.

Consider the total effective magnetic field \mathcal{B}_{MI} in the MI region. This field has contributions from several physical mechanisms; we write

$$\mathcal{B}_{MI} = \mathcal{B}_{int} + \mathcal{B}_{st} + \mathcal{B}_{SP} + \mathcal{B}_{LC}, \tag{26}$$

¹³ This is due to 2nd-order spin–spin and spin–rotation couplings to distant $|\widetilde{J}, m_J\rangle$ states.

Table 3. All non-degenerate pairs of $|m_J|=1$ states in the $\widetilde{J}=1$ manifold at $\mathcal{E}_{\mathrm{MI}}=30$ kV cm $^{-1}$ that do not involve the states $|i\rangle$ and $|l\rangle$ or a flip of m_J . The quantum numbers given are that of the largest decoupled-basis component. State labels l are as in [32] and figure 11. The quantities $\mathrm{d}f_0/\mathrm{d}\mathcal{E}_z$ give the slope of the resonance frequency with respect to the external magnetic field and electric field, respectively. Shift $\mathcal{B}_{\mathrm{mot}}$ indicates the resonance frequency shift, due to the motional field that accompanies \mathcal{E} reversal, with respect to a stray field component \mathcal{B}_y . S denotes the sensitivity to the NSM relative to the maximum possible value; it is given by $|\langle I_{1,z} \rangle_1 - \langle I_{1,z} \rangle_2|$ for the transition between states 1 and 2. f_0 indicates the transition frequency between the two states. $|\langle \cdot | \mathcal{H}_Z | \cdot \rangle|$ indicates the magnitude of the transition dipole moment between states 1 and 2. All shifts are calculated from diagonalization of the ground-state Hamiltonian (equation (7)).

		State 1				State 2			f_0	$\mathrm{d}f_0/\mathrm{d}\mathcal{B}_z$ $\mathrm{d}f_0/\mathrm{d}\mathcal{E}_z$	$\mathrm{d}f_0/\mathrm{d}\mathcal{E}_z$	Shift \mathcal{B}_{mot}	S $ \langle \cdot \mathcal{H}_Z \cdot \rangle $ [kHz]		
What flips?	l	m_J	m_{I_1}	m_{I_2}	l	m_J	m_{I_1}	m_{I_2}	kHz	$[mHz/\mu G]$	[mHz/(V/cm)]	$[\mathrm{mHz}/\mu\mathrm{G}]$	-	<i>x</i> , <i>y</i>	z
m_{I_1}	∫ e	_	_	_	j	-	+	_	119.52	+2.49	-31.50	$+4.66 \times 10^{-5}$	0.95	1.33	0.00
	h	+	+	+	k	+	_	+		-2.49		$+5.22 \times 10^{-5}$			0.00
m_{I_1}, m_{I_2}	∫ f	+	+	_	k	+	_	+	108.92	+1.52	-3.57	-1.17×10^{-4}	0.99	0.00	0.00
	g	_	_	+	j	_	+	_		-1.52		-1.23×10^{-4}			0.09
												$+1.69 \times 10^{-4}$	0.04		0.00
	h	+	+	+	f	+	+	_		-4.00					0.00

where \mathcal{B}_{int} is the intra-molecular magnetic field, \mathcal{B}_{st} is a static stray field, \mathcal{B}_{SP} is from the magnetic fields in SPB and SPC penetrating into the MI region, and \mathcal{B}_{LC} is from leakage currents in the electrode structure. Both \mathcal{B}_{int} and \mathcal{B}_{SP} change sign under \mathcal{B} modulation. Under \mathcal{M} modulation, only \mathcal{B}_{int} changes sign. We do not expect \mathcal{B}_{st} to change significantly under any of the modulations. So, in order to fully suppress the direct shifts due to stray magnetic fields, all three modulations \mathcal{E} , \mathcal{B} and \mathcal{M} are required.

However, none of these modulations help to distinguish Zeeman shifts due to \mathcal{B}_{LC} from a true NSM signal, since both reverse under E modulation. Hence, as usual for EDM experiments, it will be very important to minimize the leakage current I_{LC} . Using the standard crude approximation for a worst-case scenario of \mathcal{B}_{LC} (where all leakage current flows around a helical path between electrodes), we find that I_{LC} could conceivably need to be as low as ~ 1 nA to absolutely ensure that this systematic error is less than our anticipated statistical sensitivity. Because this may prove challenging, we discuss possible methods to reduce our sensitivity to leakage currents in section 3.4.

The magnitude of all other contributions to \mathcal{B}_{MI} can be determined from appropriate signal combinations. For example, $\mathcal{S}_{BMP}\approx 5\mathcal{B}_{st}\,$ mHz μG^{-1} determines \mathcal{B}_{st} , since B and M work together to reverse \mathcal{B}_{int} but keep the orientation of the spins. Similarly, $\mathcal{S}_{MP}\approx 5\mathcal{B}_{SP}\,$ mHz μG^{-1} determines \mathcal{B}_{SP} , since M flips the direction of the spins relative to the fields in SPB and SPC regions. Once measured, these fields can be nulled; then, by deliberately exaggerating each component separately, their residual effects on Δ_{CPV} can be measured.

Another type of undesired \mathcal{B} -field arises because the molecules move through the \mathcal{E}_{MI} -field with finite velocity $\mathbf{v} = v\hat{\mathbf{x}}$. They therefore experience a motional magnetic field,

$$\mathcal{B}_{\text{mot}} = \mathbf{v} \times \frac{\mathcal{E}}{c^2}.$$
 (27)

 \mathcal{B}_{mot} is always perpendicular to both \mathbf{v} and \mathcal{E} , i.e. nominally in the \hat{y} direction. If there is any static magnetic field with a nonzero y-component, the total magnetic field magnitude will be $\mathcal{B}_{tot} = \sqrt{\mathcal{B}_{int}^2 + (\mathcal{B}_{mot} + \mathcal{B}_{st})^2}$. This means that \mathcal{B}_{tot} will change in magnitude when \mathcal{E}_{MI} is reversed. Since the Zeeman splitting between spin up and down is proportional to \mathcal{B}_{tot} , this leads to a frequency shift under \mathcal{E}_{MI} reversal. With our experimental parameters, the resulting shift is approximately $\mathcal{B}_{st,y} \times 50$ nHz μG^{-1} . Assuming we reach our target level of residual magnetic field, $\mathcal{B}_{st} < 10 \ \mu G$, a shift of $0.5 \ \mu Hz$ is expected. However, this shift is strongly (but not completely) suppressed due to the M modulation, because the Zeeman shift due to \mathcal{B}_{mot} is nearly, but not identically, equal for transitions ej and hk. The difference in the motional-field induced shift between the two transitions is $\approx \mathcal{B}_{st,y} \times 5.6$ nHz μG^{-1} . For a field $\mathcal{B}_{st,y} = 10 \ \mu G$, this is roughly the same as our anticipated statistical sensitivity. However, as described in section 3.4, it should be possible to isolate any residual contribution from the motional field shift by employing co-magnetometry in CeNTREX.

3.3.3. Other known sources of systematic errors

We have considered several other known sources of systematic errors that have been discussed in literature on searches for *T*-violation in TIF. For example, shifts due to the Millman effect [69] (caused by

misalignment of the NMR RF field coils) reverse with *B* and *M*, and hence are suppressed only by *E* modulation. However, with good construction techniques the residual effects appear likely to be smaller than our anticipated sensitivity. Furthermore, the Millman effect can be quantified experimentally (see section 3.4 and reference [30]). Similarly, we have considered the effect of undesired phase offsets between the two RF coils, and also found the residual effects to be small compared to our anticipated sensitivity.

3.4. Internal co-magnetometry in CeNTREX

Because the risk of systematic errors from stray magnetic fields is substantial, many of the latest generation of EDM searches have employed co-magnetometers, i.e. other physical systems used to measure magnetic fields co-located with the EDM-sensitive system in both space and time. Some experiments have used different species nominally sharing the same volume [12, 68]. Others have used different internal states of the EDM-sensitive system, which have different sensitivity to the EDM and/or to magnetic fields [61, 70]. This 'internal co-magnetometer' approach [71] has the advantage of guaranteed spatial overlap between the two systems, and reduced experimental complexity.

We believe it will be possible to use different internal states of TIF to act as a type of generalized internal co-magnetometer. As we have discussed, the apparently natural choices of internal states to use for the 205 Tl NSM search are those where the 205 Tl spin flips, but all other quantum numbers remain (nominally) the same. This corresponds to the pairs $e \leftrightarrow j$ and $h \leftrightarrow k$ assumed throughout our discussion. However, it is entirely viable to instead employ pairs of states where only the 19 F spin flips, i.e. the pairs $e \leftrightarrow g$ and $e \leftrightarrow h$. As shown in table 3, these pairs of states are 2–3 times more sensitive to magnetic field effects than the usual pairs. However, they have negligible sensitivity to eT-violating effects, since the ePF nucleus has small eT and ePA. Hence, these pairs of states can act as a classic co-magnetometer. The experimental configuration remains nearly unchanged from that used for NSM detection; the primary change is that a significantly lower NMR resonance frequency, ePair of states, which will provide a novel diagnostic for systematic errors and stray fields in CeNTREX. We are still designing state preparation and readout protocols that will enable use of these pairs of states.

Even more potentially useful could be to employ the pairs of states $f \leftrightarrow k$ and $g \leftrightarrow j$. In these transitions, both nuclear spins flip simultaneously. Measurements with these pairs are nearly 2 times less sensitive to magnetic fields from leakage currents and residual shield magnetization than the original pair and more than an order of magnitude less sensitive to \mathcal{E} -induced Zeeman shifts, but have enhanced sensitivity to motional field shifts. Hence, making measurements with these pairs as well as both single spin-flip pairs will provide a wealth of information to disentangle contributions from the most important systematic error contributions we are now aware of. Employing these double spin-flip transitions will require an additional NMR RF coil to produce fields along \hat{z} . Here, because of the small transition dipole matrix element, the RF field magnitude will need to be roughly 10 times larger than for the other pairs. We are currently investigating the feasibility of using these states in CeNTREX.

4. Conclusion

As described in section 3, we anticipate a statistical sensitivity to the CPV-induced energy (Δ_{CPV}) of $\delta\Delta_{\text{CPV}}\approx 50$ nHz. This would correspond to a roughly 2500-fold improvement over the previous best measurements of the 205 Tl NSM. Taking into account the calculated relation between the NSM and underlying parameters of fundamental physics, this would in many cases correspond to a significantly improved sensitivity over the current best limits. For example, this would be sensitive to values of the QCD CPV parameter $\bar{\theta}\gtrsim 1\times 10^{-12}$, a factor of ≈ 100 smaller than current bounds [10, 12], and to a proton EDM of $d_{\rm p}\gtrsim 6\times 10^{-27}{\rm e}$ cm, a factor of ≈ 30 smaller than the current best limit [10].

Currently, measurements and optimization of the rotational cooling efficiency are underway. Once this is completed, the SPA region and then the EQL region will be attached to the beamline for testing and optimization. The MI region is under construction. The remaining regions, SPB, SPC, and FD, are under design. Once the entire apparatus is assembled and tested, we will commence measurements, with the goal to reach the target sensitivity $\delta\Delta_{\rm CPV}\lesssim 50$ nHz.

Subsequent generations of CeNTREX with considerable further improvements in sensitivity, also are anticipated. For example, we plan to implement transverse laser cooling to collimate the TlF beam [37, 39], and a continuous cryogenic buffer gas beam source [72–75] loaded by a thermal TlF beam. Preliminary estimates indicate that these improvements could increase the detected number of molecules by a factor of 30–100. In the further future, it may also be possible to slow, cool, and optically trap the TlF molecules. This could dramatically increase the interaction time per molecule, though it remains to be seen what fraction of molecules can be captured in this way. In any case, the CeNTREX approach has the potential to yield substantially improved sensitivity to flavor-neutral CPV physics in the hadronic sector.

CeNTREX may also be used to search for axions, either measuring the oscillating Schiff moment produced by the interaction with an axion dark matter particle [76] or searching for virtual axions mediating CP-violation and producing a Schiff moment in the Tl nucleus [77, 78].

Acknowledgments

We thank L R Hunter and N Clayburn for many helpful discussions, and for sharing preliminary data on optical cycling in TlF. We are grateful for support from the John TempletonFoundation, the Heising-Simons Foundation, a NIST Precision Measurement Grant, and NSF-MRI Grants PHY1827906, PHY-1827964, and PHY-1828097, and the USDOE Office of Nuclear Physics.

Appendix A. State evolution and loss between regions in CeNTREX

In this appendix, we explain in some detail how quantum states evolve as they move between the different regions of the CeNTREX beamline. Our discussion centers on the mechanisms that lead to undesired population transfer, and their likely magnitude in CeNTREX.

Unwanted state transfer is most likely to occur when the desired level undergoes an avoided crossing with an undesired level. Such avoided crossings occur in CeNTREX when a pair of states are coupled by one mechanism (e.g. hyperfine or Zeeman interactions) while their energy varies due to a separate mechanism (e.g. Stark shifts in varying \mathcal{E} -fields). A qualitative understanding of when transitions occur at a level crossing can be found via generalization of the Landau–Zener model [79]. We consider cases where the system begins in the pure state $|a\rangle$, and the time-varying energy splitting $\Delta(t)$ between $|a\rangle$ and the other state, $|b\rangle$, goes through 0. Here $\Delta(t)$ refers to the energy splitting when neglecting terms in the Hamiltonian that couple these states, $\mathcal{H}_{\rm I}$. The nonzero coupling between the two states, with strength $\hbar\Omega = \langle a|\mathcal{H}_{\rm I}|b\rangle$, leads to an avoided crossing (figure 12).

Since the character (i.e. good quantum numbers) of each state can be markedly different on either side of an avoided crossing, we label the upper (lower) state after the crossing as $|a'\rangle$ ($|b'\rangle$). The state of the system after the avoided crossing is governed by the parameter $\Gamma=\Omega^2/(\mathrm{d}\Delta/\mathrm{d}t)$. The probability to end in $|b'\rangle$ is large, i.e. the evolution is adiabatic, when $\Gamma\gg 1$. Conversely, the probability to end in $|a'\rangle$ is large, i.e. the evolution is sudden, when $\Gamma\ll 1$. In the intermediate range, when $\Gamma\sim 1$, the final state is generally a superposition of $|a'\rangle$ and $|b'\rangle$, with relative amplitudes that depend critically on the details of the system.

Centrex is designed so that molecular states evolve either adiabatically, $\Gamma\gg 1$, or suddenly, $\Gamma\ll 1$, through avoided crossings that occur when traversing between functional regions. Thus, the state before and after any such traversal should be deterministically pure. Throughout the experiment, the local $\boldsymbol{\mathcal{E}}$ -field is always sufficiently large to define a local quantization axis $\hat{\zeta}$, whose direction changes continuously along the molecular trajectory. In the frame that is co-moving with the molecules, couplings between desired and undesired states arise from hyperfine interactions, Zeeman interactions, or changes in $\boldsymbol{\mathcal{E}}$ -field direction.

Earlier experiments using 205 TlF to search for T-violation noted severe problems with deterministic state transfer when molecules move from regions of low \mathcal{E} to high \mathcal{E} . This is likely to occur because of the high density of avoided crossings in this transition between regimes [30, 32]. Hence, throughout the CeNTREX apparatus we ensure that $\mathcal{E} > 50 \text{ V cm}^{-1}$, such that only transitions between mid- and high-field regimes are relevant. There are two classes of transition regions where deterministic evolution of pure states is nontrivial in CeNTREX. The first class refers to transitions between the electrostatic lens and state preparation regions A and B; the second class refers to transitions between the MI region and state preparation regions B and C. We discuss each in some detail here.

The \mathcal{E} -fields in the SPA and SPB regions ($\sim 100 \text{ V cm}^{-1}$ maximum) and in the transitions between these and the EQL region ($\sim 50 \text{ V cm}^{-1}$ minimum) lie in the mid-field regime; in the EQL region, $\mathcal{E} \sim 10{\text -}30 \text{ kV cm}^{-1}$ is in the high-field regime (see section 1.2). In the transition between mid- and high-field regimes, several subtle but important effects arise due to the coupling between molecular rotation **J** and nuclear spins \mathbf{I}_1 and \mathbf{I}_2 (described by the terms proportional to c_1 and c_2 in equation (7)). First, in the mid-field regime (see section 1.2), the molecular eigenstates are only nominally described by the mid-field basis states $|J, m_J\rangle |I_t, m_{I_t}\rangle$ (for $m_J = 0$). This means that molecules nominally prepared in the desired state $|J = 2, m_J = 0\rangle |I_t = 0, m_{I_t} = 0\rangle$, in the SPA region, are actually prepared in an eigenstate $|\psi_{\text{SPA}}\rangle$ that has a small admixture of states with $m_J = \pm 1$. For example, when $\mathcal{E} \sim 50 \text{ V cm}^{-1}$, we find

$$|\psi_{\text{SPA}}\rangle \approx |J=2, m_{J}=0\rangle |I_{\text{t}}=0, m_{I_{\text{t}}}=0\rangle + \eta |J=2, m_{J}=1\rangle |I_{\text{t}}=1, m_{I_{\text{t}}}=-1\rangle - \eta |J=2, m_{J}=-1\rangle |I_{\text{t}}=1, m_{I_{\text{t}}}=+1\rangle,$$
(28)

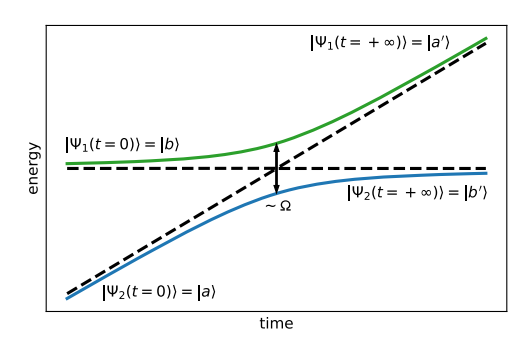


Figure 12. Energy level diagram for a two-level system with an avoided crossing. Black dashed lines show the energies when $\mathcal{H}_1=0$; solid lines show energies in the presence of nonzero coupling strength $\hbar\Omega$. Adiabatic (diabatic) evolution corresponds to initial population in one state remaining on the solid (dashed) lines as the system evolves through the avoided crossing.

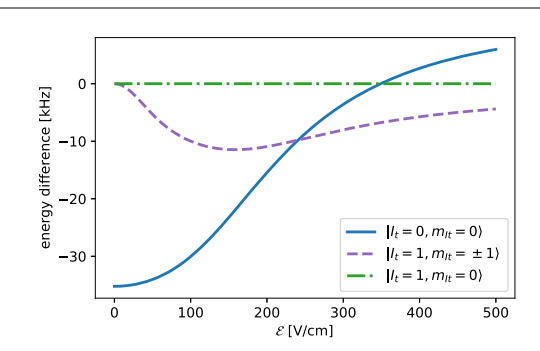


Figure 13. Relative energies of the nuclear spin states within the $J=2, m_J=0$ manifold, versus \mathcal{E} -field magnitude (with $\mathcal{B}=0$). The energy of the $|I_t=1, m_{I_t}=0\rangle$ state is defined as the reference energy at every value of \mathcal{E} . Level crossings occur at ~ 240 and 350 V cm⁻¹. If the \mathcal{B} -field is non-zero or the \mathcal{E} -field is rotating, the different spin states will be coupled and the crossings will be avoided.

where the mixing coefficient η is determined by the strength of the hyperfine interaction compared to the Stark shift between states with different m_J : $\eta \approx \hbar \Omega_{\rm hf}/\Delta E_{\rm S} \sim 0.1$. Here, the nonzero value of η arises from the spin–rotation terms in $\mathcal{H}_{\rm I}$, which couple states with $\Delta m_J = \pm 1 = -\Delta m_{I_{\rm t}}$. By contrast, in the high-field regime of the EQL, states with different values of m_J are very distant. Hence, here the true eigenstates $|\psi_{\rm EQL}\rangle$, corresponding to the desired states $|\widetilde{J}, m_J = 0\rangle |I_{\rm t} = 0, m_{I_{\rm t}} = 0\rangle$, have negligibly small admixtures of states with $m_J \neq 0$ or $I_{\rm t} \neq 0$ (i.e. $\eta \ll 1$).

Second, as a function of \mathcal{E} in the transition from mid- to high-field regimes, the (nominal) $|J=2,m_J=0\rangle$ eigenstates with different spin content undergo a few level crossings (figure 13). This occurs as the spins fully decouple from rotation in any $m_I=0$ rotational state.

Finally, in the mid-field regime, rotation of the \mathcal{E} -field can cause transitions between states with (nominally) different nuclear spin configurations. The source of these transitions can be understood qualitatively: in the mid-to-high field regime, J is strongly coupled to \mathcal{E} and must reorient appropriately as the electric field rotates. If the rotation of J is too fast for the coupled nuclear spins to follow, their orientation with respect to the quantization axis provided by \mathcal{E} may change so that the spins end up in a different state relative to the local $\hat{\zeta}$ -axis.

To describe couplings induced by \mathcal{E} -field rotation, we follow the approach of Wall $et\ al\ [80]$. We write the Hamiltonian in a co-moving frame with axes (ξ, v, ζ) , where \mathcal{E} defines the local direction of the ζ -axis at all points along the molecular trajectory. In this frame, $\hat{\zeta}$ may point in any direction relative to a set of laboratory-fixed axes, and its direction rotates continuously as the molecules move along their path in the lab. Consider what happens when a molecule moves from the low field in the SPA region to the high field in the EQL region. In the SPA region, \mathcal{E} is parallel to the average molecular beam direction, \hat{Z} . The quadrupole field is always in the X-Y plane in this frame; here we consider a particular molecular trajectory such that the direction of \mathcal{E} inside the lens is along \hat{X} . (Analogous arguments hold for other trajectories).

To keep the \mathcal{E} -field along $\hat{\zeta}$, we rotate co-moving coordinate system about the laboratory Y-axis, by an angle $\theta(t) = \arctan\left(\frac{\mathcal{E}_{\text{EQL}}(t)}{\mathcal{E}_{\text{SPA}}(t)}\right)$. Here, $\mathcal{E}_{\text{EQL}}(t)$ is the magnitude of the transverse field due to the EQL, and $\mathcal{E}_{\text{SPA}}(t)$ that of the axial field due to the ring electrodes in the SPA region. As the molecule moves between

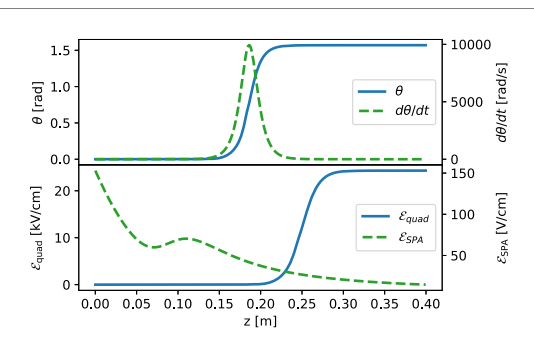


Figure 14. Top: angle *θ* between the \mathcal{E} -field direction $\hat{\zeta}$ and the lab frame *Z*-axis, and its rate of change over time $d\theta/dt$, for a molecule with typical velocity $\mathbf{v} = v_Z \hat{Z}$ and $v_Z = 184$ m s⁻¹, vs *Z*-position. Bottom: the magnitudes of the \mathcal{E} -fields in the transition region between the SPL and EQL regions, as a function of *Z*-position. The field due to the SPA region electrodes, \mathcal{E}_{SPA} , is along the length of the apparatus (*Z*); the direction of the field due to the lens electrodes, \mathcal{E}_{EQL} , is taken to be along *X* in the lab frame.

the regions, it will see the electric field rotate as \mathcal{E}_{SPA} diminishes and \mathcal{E}_{EQL} increases (see figure 14). The unitary rotation matrix that takes us from the lab frame to the co-moving frame is given by

$$U_{R}(\theta) = \exp(-i\theta(t)\mathbf{F} \cdot \hat{\mathbf{Y}}), \tag{29}$$

where $\mathbf{F} = \mathbf{J} + \mathbf{I}_1 + \mathbf{I}_2$ is the total angular momentum. The time-evolution in this rotated frame is given by

$$i\hbar \frac{\mathrm{d}|\psi\rangle_{\mathrm{R}}}{\mathrm{d}t} = \mathcal{H}_{\mathrm{eff}}|\psi\rangle_{\mathrm{R}} = \left(U_{\mathrm{R}}^{\dagger}\mathcal{H}U_{\mathrm{R}} - i\hbar U_{\mathrm{R}}^{\dagger}\frac{\mathrm{d}U_{\mathrm{R}}}{\mathrm{d}t}\right)|\psi_{\mathrm{R}}\rangle,\tag{30}$$

where \mathcal{H} is the Hamiltonian in the lab frame and $|\psi_R\rangle$ is the state vector in the rotated frame. The term $U_R^{\dagger}\mathcal{H}U_R$ is the usual Hamiltonian for TlF with a time-varying but non-rotating \mathcal{E} -field along $\hat{\zeta}$. The other term, $U_R^{\dagger}\frac{dU_R}{dt}$, contains the effects due to the rotation of \mathcal{E} . This term can be written as

$$\mathcal{H}_{\text{int}}^{(\text{eff})} = -i\hbar U_{\text{R}}^{\dagger} \frac{dU_{\text{R}}}{dt} = -\hbar \left(J_{\text{Y}} + I_{1,\text{Y}} + I_{2,\text{Y}} \right) \frac{d\theta}{dt}.$$
 (31)

Due to the spin-rotation interaction, the matrix elements of J_Y between $|\psi_{\rm SPA}\rangle$ and the undesired spin triplet states, nominally $|J=2,m_J=0\rangle$ $|I_{\rm t}=1,m_{I_{\rm t}}=\mp 1\rangle$, are non-zero; their magnitude is $\Omega \sim \eta \frac{{\rm d}\theta}{{\rm d}t}$, where η is the mixing coefficient from equation (28). Due to this off-diagonal coupling, the level crossings in figure 13 become avoided crossings. Hence, fully adiabatic evolution here would result in our desired $I_{\rm t}=0$ state evolving into an undesired $I_{\rm t}=1$ state, as shown in figure 12. Instead, here we want the state evolution to be sudden/fully diabatic to maintain $I_{\rm t}=0$. To avoid population loss, we thus require ${\rm d}\Delta/{\rm d}t\gg\eta^2\dot{\theta}^2$. This condition only needs to be fulfilled when the coupled levels are close in energy, i.e. when ${\cal E}\approx 200-400$ V cm⁻¹ (see figure 13). This is achieved in practice by allowing ${\cal E}_{\rm SPA}$ to decay to ≈ 50 V cm⁻¹ before ${\cal E}_{\rm EQL}$ starts to rapidly increase. The ${\cal E}$ -field is then almost entirely in the transverse direction, i.e. not rotating quickly, by the time the level-crossing occurs (figure 14).

We note in passing that the axial-to-transverse field configuration in CeNTREX has not been used in previous 205 TlF experiments. If only transverse fields are used, inevitably some large fraction of molecular trajectories travel through a position where $\mathcal{E}=0$ and undesired transitions are strong. Our approach mimics that of reference [81], but using \mathcal{E} rather than \mathcal{B} as the quantizing field.

Magnetic fields can also couple the desired $I_{\rm t}=0$, $m_{I_{\rm t}}=0$ state to $I_{\rm t}=1$ states with $m_{I_{\rm t}}=0$ ($m_{I_{\rm t}}=\pm 1$) when $\mathcal{B}_Z\neq 0$ ($\mathcal{B}_{X,Y}\neq 0$). To reduce this effect, in CeNTREX we will apply shim coils to cancel typical ambient lab fields in the regions of transition into and out of the EQL region. With cancellation by a factor of $\gtrsim 10$, such that $\mathcal{B}\lesssim 0.05\,$ mG, the Zeeman coupling strengths are in the range $\Omega_Z\lesssim 0.1\,$ kHz. When the condition needed to avoid transitions from $\boldsymbol{\mathcal{E}}$ -rotation given above are satisfied, the rate of change of the level splittings as molecules enter the very strong $\boldsymbol{\mathcal{E}}$ -field of the lens, $\mathrm{d}\Delta/\mathrm{d}t$, is sufficiently large compared to Ω_Z such that the evolution is fully diabatic. Numerical simulations indicate a loss of <1% along any molecular trajectory. Hence, under these conditions the quantum numbers $I_{\rm t}=0$, $m_{I_{\rm t}}=0$ are preserved as molecules enter and exit the EQL region.

The transition from the EQL region to SPB region is mostly similar to the transition from the SPA region to the EQL region. The primary difference is the requirement in the SPB region to have a uniform electric field $\mathcal{E}_{SPB} = \mathcal{E}_{SPB}\hat{z}$, along with a substantial magnetic field, $\mathcal{B}_{SPB} = \mathcal{B}_{SPB}\hat{z}$, where $\mathcal{B}_{SPB} \approx 10-20\,$ G. Here, we are describing fields in the (x, y, z) 'interaction region' coordinate system. These fields can be reached by first diabatically rotating from the large transverse lens field \mathcal{E}_{EQL} to a weak axial field $\mathcal{E}\|\hat{Z}$, then

adiabatically rotating into the uniform transverse field $\mathcal{E}_{SPB} \| \hat{z}$. Throughout the second \mathcal{E} rotation, \mathcal{E} remains in the range 50–100 V cm⁻¹ while \mathcal{B}_z slowly rises, from its initial value of (nominally) zero to \mathcal{B}_{SPB} . Though the details remain to be worked out, this scheme should ensure deterministic population of the desired state in the EQL–SPB transition.

The last class of traversals in CeNTREX occurs between the SPB and MI regions (or, similarly aside from the reversed sequence, the MI and SPC regions). Here, the \mathcal{B} -field must transform from \mathcal{B}_{SPB} to zero, and the \mathcal{E} -field can remain in the same \hat{z} direction but must make the transition from low- to high-field regimes. This can again be accomplished by adiabatically ramping \mathcal{B} to zero while maintaining $\mathcal{E} \approx 50-100 \text{ V cm}^{-1}$ along \hat{z} . Then, a sudden rise to $\mathcal{E} \gg 500 \text{ V cm}^{-1}$ will maintain the spin quantum numbers for molecules coming into/out of the MI region. During these traversals, there is a possibility of undesired transitions between different nuclear spin states, if the \mathcal{B} -field is not fully parallel to the \mathcal{E} -field. Whether or not these transitions are likely to pose a problem, and if so how to mitigate them, is currently being investigated. We note that in prior experiments with TIF [32, 52], this issue was appreciated but not fully under control.

While keeping track of state evolution across level crossings may appear daunting, it is analogous to even more complex schemes that have been applied efficiently in other molecular systems [82]. We believe that our detailed understanding of and control over these issues will be necessary to understand and minimize systematic errors in CeNTREX.

ORCID iDs

O Grasdijk https://orcid.org/0000-0001-6427-4164

References

- [1] Landau L 1957 On the conservation laws for weak interactions Nucl. Phys. 3 127-31
- [2] Christenson J H, Cronin J W, Fitch V L and Turlay R 1964 Evidence for the 2π decay of the K_2^0 meson Phys. Rev. Lett. 13 138
- [3] Tanabashi M et al 2018 Review of particle physics Phys. Rev. D 98 030001
- [4] Peccei R D 1995 CP violation: a theoretical review (arXiv:hep-ph/9508389)
- [5] Kobayashi M and Maskawa T 1973 CP-violation in the renormalizable theory of weak interaction Prog. Theor. Phys. 49 652-7
- [6] Canetti L, Drewes M and Shaposhnikov M 2012 Matter and antimatter in the universe New J. Phys. 14 095012
- [7] Sakharov A D 1991 Violation of CP invariance, C asymmetry, and baryon asymmetry of the universe Sov. Phys. Usp. 34 392
- [8] Pospelov M and Ritz A 2005 Electric dipole moments as probes of new physics Ann. Phys., NY 318 119-69
- [9] Pospelov M and Adam R 1999 The theta term in QCD sum rules and the electric dipole moment of the vector meson *Nucl. Phys.* B 558 243-58
- [10] Graner B et al 2016 Reduced limit on the permanent electric dipole moment of 199 Hg Phys. Rev. Lett. 116 161601
- [11] Baker C A et al 2006 Improved experimental limit on the electric dipole moment of the neutron Phys. Rev. Lett. 97 131801
- [12] Abel C et al 2020 Measurement of the permanent electric dipole moment of the neutron Phys. Rev. Lett. 124 081803
- [13] Peccei R D and Quinn H R 1977 CP conservation in the presence of pseudoparticles *Phys. Rev. Lett.* 38 1440–3
- [14] Preskill J, Wise M B and Wilczek F 1983 Cosmology of the invisible axion Phys. Lett. B 120 127-32
- [15] Ipser J and Sikivie P 1983 Can galactic halos be made of axions? Phys. Rev. Lett. 50 925-7
- [16] Braine T et al 2020 Extended search for the invisible axion with the axion dark matter experiment Phys. Rev. Lett. 124 101303
- [17] Graham P W, Irastorza I G, Lamoreaux S K, Lindner A and van Bibber K A 2015 Experimental searches for the axion and axion-like particles *Annu. Rev. Nucl. Part. Sci.* 65 485–514
- [18] Schiff L I 1963 Measurability of nuclear electric dipole moments Phys. Rev. 132 2194
- [19] Pospelov M E and Khriplovich I B 1991 Electric dipole moment of the W boson and the electron in the Kobayashi–Maskawa model Sov. J. Nucl. Phys 53 638–40
- [20] Safronova M S, Budker D, DeMille D, Kimball D F J, Derevianko A and Clark C W 2018 Search for new physics with atoms and molecules Rev. Mod. Phys. 90 025008
- [21] Ginges J S M and Flambaum V V 2004 Violations of fundamental symmetries in atoms and tests of unification theories of elementary particles *Phys. Rep.* **397** 63–154
- [22] Khriplovich I B and Lamoreaux S 1997 CP Violation without Strangeness (Berlin: Springer)
- [23] Flambaum V V and Dzuba V A 2020 Electric dipole moments of atoms and molecules produced by enhanced nuclear Schiff moments Phys. Rev. A 101 042504
- [24] Flambaum V V, Dzuba V A and Tran Tan H B 2020 Time- and parity-violating effects of the nuclear Schiff moment in molecules and solids Phys. Rev. A 101 042501
- [25] Titov A V, Mosyagin N S, Petrov A N and Isaev T A 2005 Two-step method for precise calculation of core properties in molecules Int. J. Quantum Chem. 104 223–39
- [26] Petrov A N, Mosyagin N S, Isaev T A, Titov A V, Ezhov V F, Eliav E and Kaldor U 2002 Calculation of *P*, *T*-odd effects in ²⁰⁵TlF including electron correlation *Phys. Rev. Lett.* **88** 073001
- [27] Abe M, Tsutsui T, Ekman J, Hada M and Das B 2020 Accurate determination of the enhancement factor X for the nuclear Schiff moment in ²⁰⁵TlF molecule based on the four-component relativistic coupled-cluster theory Mol. Phys. 118 e1767814
- [28] Khriplovich I B 1991 Parity Nonconservation in Atomic Phenomena (London: Gordon and Breach)
- [29] Cho D, Sangster K and Hinds E A 1989 Tenfold improvement of limits on T violation in thallium fluoride Phys. Rev. Lett. 63 2559
- [30] Cho D, Sangster K and Hinds E A 1991 Search for time-reversal-symmetry violation in thallium fluoride using a jet source Phys. Rev. A 44 2783
- [31] Sandars P G H 1967 Measurability of the proton electric dipole moment Phys. Rev. Lett. 19 1396

- [32] Wilkening D A, Ramsey N F and Larson D J 1984 Search for P and T violations in the hyperfine structure of thallium fluoride Phys. Rev. A 29 425
- [33] Kozlov M G and Labzowsky L N 1995 Parity violation effects in diatomics J. Phys. B: At. Mol. Opt. Phys. 28 1933
- [34] Huber K P and Herzberg G 2013 Molecular Spectra and Molecular Structure: IV. Constants of Diatomic Molecules (Berlin: Springer)
- [35] Afeefy H Y, Liebman J F and Stein S E Neutral Thermochemical Data (NIST ChemistryBook, NIST Standard Reference Database Number 69 5 September 2020) (NIST) https://doi.org/10.18434/T4D303
- [36] Brown J M and Carrington A 2003 Rotational Spectroscopy of Diatomic Molecules (Cambridge: Cambridge University Press)
- [37] Norrgard E B, Edwards E R, McCarron D J, Steinecker M H, DeMille D, Alam S S, Peck S K, Wadia N S and Hunter L R 2017 Hyperfine structure of the $B^3\Pi_1$ state and predictions of optical cycling behavior in the $X \to B$ transition of TlF *Phys. Rev.* A 95 062506
- [38] Meijer G and Sartakov B G 2020 Λ doubling in the $B^3\Pi_1$ state of TIF Phys. Rev. A 101 042506
- [39] Hunter L R, Peck S K, Greenspon A S, Alam S S and DeMille D 2012 Prospects for laser cooling TlF Phys. Rev. A 85 012511
- [40] Ramsey N F 1950 A molecular beam resonance method with separated oscillating fields Phys. Rev. 78 695-9
- [41] Ramsey N F and Silsbee H B 1951 Phase shifts in the molecular beam method of separated oscillating fields Phys. Rev. 84 506
- [42] Hutzler N R, Lu H-I and Doyle J M 2012 The buffer gas beam: an intense, cold, and slow source for atoms and molecules *Chem. Rev.* 112 4803–27
- [43] Clayburn N B, Wright T H, Norrgard E B, DeMille D and Hunter L R 2020 Measurement of the molecular dipole moment and the hyperfine and omega doublet splittings of the $B^3\Pi_1$ state of thallium fluoride (arXiv:2007.16101)
- [44] Berkeland D J and Boshier M G 2002 Destabilization of dark states and optical spectroscopy in Zeeman-degenerate atomic systems Phys. Rev. A 65 033413
- [45] Shuman E S, Barry J F, Glenn D R and DeMille D 2009 Radiative force from optical cycling on a diatomic molecule Phys. Rev. Lett. 103 223001
- [46] Yeo M, Hummon M T, Collopy A L, Yan B, Hemmerling B, Chae E, Doyle J M and Ye J 2015 Rotational state microwave mixing for laser cooling of complex diatomic molecules *Phys. Rev. Lett.* 114 223003
- [47] Tarbutt M R, Sauer B E, Hudson J J and Hinds E A 2013 Design for a fountain of YbF molecules to measure the electron's electric dipole moment New J. Phys. 15 053034
- [48] Hunter L R and Clayburn N B 2019 private communication Physics Department, Amherst College, Amherst, Massachusetts 01002, USA
- [49] Budker D, Kimball D F and DeMille D P 2004 Atomic Physics: An Exploration through Problems and Solutions (Oxford: Oxford University Press)
- [50] Bennewitz H G, Paul W and Schlier C 1955 Fokussierung polarer moleküle Z. Phys. 141 6–15
- [51] Berg R A, Wharton L, Klemperer W, Büchler A and Stauffer J L 1965 Determination of electronic symmetry by electric deflection: LiO and LaO J. Chem. Phys. 43 2416–21
- [52] Cho V A and Bernstein R B 1991 Tight focusing of beams of polar polyatomic molecules via the electrostatic hexapole lens *J. Phys. Chem.* **95** 8129–36
- [53] Hinds E A and Sandars P G H 1980 Experiment to search for *P*-and *T*-violating interactions in the hyperfine structure of thallium fluoride *Phys. Rev.* A 21 480
- [54] Jiles D 2015 Introduction to Magnetism and Magnetic Materials 3rd edn (Boca Raton, FL: CRC Press)
- [55] Walter R 1923 Die elektrische Festigkeit am Rande des Plattenkondensators Arch. Elektrotechnik 12 1–15
- [56] Kuffel E, Zaengl W S and Kuffel J 2000 High Voltage Engineering Fundamentals 2nd edn (Oxford: Newnes)
- [57] Lamoreaux S K 1999 Feeble magnetic fields generated by thermal charge fluctuations in extended metallic conductors: implications for electric-dipole moment experiments *Phys. Rev.* A 60 1717–20
- [58] Kornack T W, Smullin S J, Lee S-K and Romalis M V 2007 A low-noise ferrite magnetic shield Appl. Phys. Lett. 90 223501
- [59] Lee S-K and Romalis M V 2008 Calculation of magnetic field noise from high-permeability magnetic shields and conducting objects with simple geometry J. Appl. Phys. 103 084904
- [60] Kirilov E et al 2013 Shot-noise-limited spin measurements in a pulsed molecular beam Phys. Rev. A 88 013844
- [61] Andreev V et al (ACME Collaboration) 2018 Improved limit on the electric dipole moment of the electron Nature 562 355-60
- [62] Lindsay B G, Smith K A and Dunning F B 1991 Control of long-term output frequency drift in commercial dye lasers *Rev. Sci. Instrum.* 62 1656–7
- [63] Jaffe S M, Rochon M and Yen W M 1993 Increasing the frequency stability of single-frequency lasers Rev. Sci. Instrum. 64 2475–81
- [64] Zhao W Z, Simsarian J E, Orozco L A and Sprouse G D 1998 A computer-based digital feedback control of frequency drift of multiple lasers Rev. Sci. Instrum. 69 3737–40
- [65] Rossi A, Biancalana V, Mai B and Tomassetti L 2002 Long-term drift laser frequency stabilization using purely optical reference Rev. Sci. Instrum. 73 2544–8
- [66] Zi F, Wu X, Zhong W, Parker R H, Yu C, Budker S, Lu X and Müller H 2017 Laser frequency stabilization by combining modulation transfer and frequency modulation spectroscopy Appl. Opt. 56 2649–52
- [67] Lasner Z and DeMille D 2018 Statistical sensitivity of phase measurements via laser-induced fluorescence with optical cycling detection Phys. Rev. A 98 053823
- [68] Regan B C, Commins E D, Schmidt C J and DeMille D 2002 New limit on the electron electric dipole moment Phys. Rev. Lett. 88 071805
- [69] Millman S 1939 On the determination of the signs of nuclear magnetic moments by the molecular beam method of magnetic resonance Phys. Rev. 55 628
- [70] Eckel S, Hamilton P, Kirilov E, Smith H W and DeMille D 2013 Search for the electron electric dipole moment using Ω-doublet levels in PbO Phys. Rev. A 87 052130
- [71] DeMille D, Bay F, Bickman S, Kawall D, Hunter L, Krause D Jr, Maxwell S and Ulmer K 2001 Search for the electric dipole moment of the electron using metastable PbO AIP Conf. Proc. 596 72–83
- [72] Patterson D and Doyle J M 2007 Bright, guided molecular beam with hydrodynamic enhancement J. Chem. Phys. 126 154307
- [73] Patterson D, Rasmussen J and Doyle J M 2009 Intense atomic and molecular beams via neon buffer-gas cooling New J. Phys. 11
- [74] Patterson D and Doyle J M 2015 A slow, continuous beam of cold benzonitrile Phys. Chem. Chem. Phys. 17 5372-5
- [75] Singh V, Samanta A K, Roth N, Gusa D, Ossenbrüggen T, Rubinsky I, Horke D A and Küpper J 2018 Optimized cell geometry for buffer-gas-cooled molecular-beam sources *Phys. Rev.* A 97 032704

- [76] Stadnik Y V and Flambaum V V 2014 Axion-induced effects in atoms, molecules, and nuclei: parity nonconservation, anapole moments, electric dipole moments, and spin-gravity and spin-axion momentum couplings *Phys. Rev.* D 89 043522
- [77] Stadnik Y V, Dzuba V A and Flambaum V V 2018 Improved limits on axionlike-particle-mediated *P, T*-violating interactions between electrons and nucleons from electric dipole moments of atoms and molecules *Phys. Rev. Lett.* 120 013202
- [78] Dzuba V A, Flambaum V V, Samsonov I B and Stadnik Y V 2018 New constraints on axion-mediated P, T-violating interaction from electric dipole moments of diamagnetic atoms Phys. Rev. D 98 035048
- [79] Wittig C 2005 The Landau—Zener formula J. Phys. Chem. B 109 8428–30
- [80] Wall T E, Tokunaga S K, Hinds E A and Tarbutt M R 2010 Nonadiabatic transitions in a Stark decelerator Phys. Rev. A 81 033414
- [81] Wood C S, Bennett S C, Cho D, Masterson B P, Roberts J L, Tanner C E and Wieman C E 1997 Measurement of parity nonconservation and an anapole moment in cesium *Science* 275 1759–63
- [82] Lang F, Straten P v d, Brandstätter B, Thalhammer G, Winkler K, Julienne P S, Grimm R and Hecker Denschlag J 2008 Cruising through molecular bound-state manifolds with radiofrequency *Nat. Phys.* 4 223–6